

Alma Mater Studiorum Università di Bologna
Archivio istituzionale della ricerca

Candidate cave entrances in a planetary analogue evaporite karst (Cordillera de la Sal, Chile): A remote sensing approach and ground-truth reconnaissance

This is the final peer-reviewed author's accepted manuscript (postprint) of the following publication:

Published Version:

Candidate cave entrances in a planetary analogue evaporite karst (Cordillera de la Sal, Chile): A remote sensing approach and ground-truth reconnaissance / Pisani, Luca; De Waele, Jo. - In: GEOMORPHOLOGY. - ISSN 0169-555X. - STAMPA. - 389:(2021), pp. 107851.1-107851.20. [10.1016/j.geomorph.2021.107851]

Availability:

This version is available at: <https://hdl.handle.net/11585/828342> since: 2021-07-19

Published:

DOI: <http://doi.org/10.1016/j.geomorph.2021.107851>

Terms of use:

Some rights reserved. The terms and conditions for the reuse of this version of the manuscript are specified in the publishing policy. For all terms of use and more information see the publisher's website.

This item was downloaded from IRIS Università di Bologna (<https://cris.unibo.it/>).
When citing, please refer to the published version.

(Article begins on next page)

This is the final peer-reviewed accepted manuscript of:

Luca Pisani, Jo De Waele, Candidate cave entrances in a planetary analogue evaporite karst (Cordillera de la Sal, Chile): A remote sensing approach and ground-truth reconnaissance, *Geomorphology*, Volume 389, 2021, 107851

The final published version is available online at:
<https://doi.org/10.1016/j.geomorph.2021.107851>

Terms of use:

Some rights reserved. The terms and conditions for the reuse of this version of the manuscript are specified in the publishing policy. For all terms of use and more information see the publisher's website.

This item was downloaded from IRIS Università di Bologna (<https://cris.unibo.it/>)

When citing, please refer to the published version.

Candidate cave entrances in a planetary analogue evaporite karst (Cordillera de la Sal, Chile): a remote sensing approach and ground-truth reconnaissance

Luca Pisani^{1*} and Jo De Waele^{1,2}

¹ University of Bologna, Department of Biological, Geological and Environmental Sciences

² La Venta Esplorazioni Geografiche, Treviso, Italy

* Corresponding author

E-mail addresses: lucapiso94@gmail.com (L. Pisani); jo.dewaele@unibo.it (J. De Waele)

ABSTRACT

The Cordillera de la Sal (CDS) is a NNE-SSW elongated fold-and-thrust belt several km wide and over 100 km long located in the hyper-arid climate of the Atacama Desert. This ridge contains important Oligocene-Miocene continental sediments including thick interbedded salt rock units which form extensive outcrops. Despite the rare occurrence of rain events, these salt rock beds host well-developed and scientifically interesting underground cave systems, perfectly adapted to the contemporary drainage network. The complete lack of vegetation makes this area a perfect analogue to extraterrestrial evaporite karst areas. A remote sensing analysis of 600 km² of Pleiades images (acquired in 2018 by courtesy of European Space Agency) at a spatial resolution of 0.5 m (panchromatic) and 2 m (RGB and near-infrared bands) and DTMs extracted from stereographic couples has allowed to map the lithological units, the drainage network, and the candidate cave entrances (CCEs) of most of the Cordillera de la Sal.

The study area has been divided in eight morpho-structural units, based on our geological and geomorphological mapping. An Analytic Hierarchy Process (AHP) was used to classify the CCE potential of these karst zones into four classes: low, medium, high, and very high potential of finding new caves. This remote-sensing derived CCEs inventory has been ground truthed with two

27 testing datasets (101 points): i) confronting the cave register based on explorations carried out prior
28 to this analysis, and ii) with a field-based validation in completely unexplored areas. These ground-
29 truthing methods support the quality and reliability of our remote sensing-derived CCEs, with
30 accuracies of 71% and 83%, respectively.

31 With this integrated remote-sensing and ground-truthing approach, we highlight that CCEs
32 identification by image analysis and GIS processing appears reliable for speleological explorations
33 in the CDS and might be a valuable tool also for objective decision-making in the search of caves
34 and potential areas susceptible to karst formation on other planetary bodies.

35

36 **Keywords:** halite caves; karst geomorphology; speleology; Pleiades satellite images; GIS

37

38 **1. Introduction**

39 Remote sensing offers the possibility to investigate large and inaccessible areas by indirect means
40 (Campbell and Wynne, 2011; Lillesand et al., 2015; Emery and Camps, 2017). The most common,
41 versatile, and accessible forms of remote sensing make use of aerial photographs and satellite
42 imagery, both of which exploit passive sensors to measure the radiation transferred (reflected,
43 emitted, and transmitted) from the earth's surface within specific bands of the electromagnetic
44 spectrum (Schowengerdt, 2006; Emery and Camps, 2017).

45 Satellite or aerial images have been used for geological, environmental, economic and urbanistic
46 applications like mapping, monitoring and catastrophic geo-hazard assessment, because of their
47 ability to survey large, remote and sometimes inaccessible terrains without coming into physical
48 contact with the target objects (Jensen, 2015; Lillesand et al., 2015). Recent developments in
49 satellite engineering sciences and spacecraft technology, together with open access data policies,
50 allow almost the whole Earth's surface to be covered by high-resolution (HR) to very-high-
51 resolution (VHR) images freely available through software platforms such as *Google Earth*.
52 However, these computer applications typically permit optical observations only in the visible RGB

53 spectrum window (390 nm – 700 nm), without the possibility of handling data and processing them
54 in a GIS environment for detailed quantitative analysis. Nevertheless, Sentinel Hub satellite images
55 offers free multispectral products at 10-60 m of ground resolution, allowing multitemporal and
56 high-resolution analysis.

57 Data processing with image elaboration and GIS software lead to vast opportunities in the
58 geomorphological and geological fields, allowing detailed investigations to be carried out, which
59 can be functional also to speleological research and karst sciences. These methods are also the only
60 possible for detecting surface morphologies on other planetary bodies (e.g., Palafox et al., 2017;
61 Wang et al., 2018; Silburt et al., 2019), and are actually used to find Candidate Cave Entrances
62 (CCEs) for future robotic cave exploration missions on both the Moon and Mars (Cushing, 2012;
63 Titus et al., 2021a, 2021b).

64 Most remote sensing applications in karst terrains are focused on sinkhole detection, morpho-
65 structural analysis, and monitoring for geohazard quantification in carbonate and evaporitic
66 sequences (Florea, 2005; Gutiérrez et al., 2008, 2011; Galve et al., 2009a, 2009b, 2011; Pepe and
67 Parise, 2014; Ozturk et al., 2018; Panno and Luman, 2018; Lipar et al., 2019; Menezes et al., 2020).
68 Identifying and mapping sinkholes, skylights, sinking streams and their evolution in populated areas
69 is therefore a challenging and valuable task, useful for managing practices and predicting and
70 mitigating natural and anthropogenic risks in karst areas (Gutiérrez et al., 2014).

71 Remote sensing techniques can also be applied for speleological research in remote areas of the
72 world or for assessing potential underground voids on extra-terrestrial bodies. Although rarely used
73 on Earth, in some cases these techniques have been useful for rapidly identifying possible cave
74 entrances in densely forested areas using Lidar-derived DEMs (Weishampel et al., 2011; Moyes and
75 Montgomery, 2019). Especially thermal cave detection techniques are promising for identifying
76 thermal contrasts between cave entrances or shelters and the areas more exposed to direct sunlight
77 (Rinker, 1975; Wynne et al., 2008). These techniques have especially been used to identify CCEs in
78 volcanic terrains on Mars, probably related to possible lava tubes: on Arsia Mons (Cushing et al.,

2007), Ascræus Montes, Pavonis, and Hadriaca Patera and many other areas on Mars (Léveillé and Datta, 2010; Cushing, 2012). On the Moon the presence of intact lava tubes has been confirmed using the SELENE Lunar Radar Sounder on Marius Hills (Kaku et al., 2017), in areas where GRAIL gravimetric measurements also suggested the presence of large underground voids (Chappaz et al., 2017). See the review paper by Sauro et al. (2020) for a recent overview on Martian and Lunar lava tubes.

Evaporitic karst terrains are also susceptible to the presence of caves related to dissolution processes and are widely recognized in our solar system, and especially on Mars, such as Juventae Chasma (Baioni and Tramontana, 2017), Tithonium Chasma (Baioni et al., 2009), Iani Chaos (Baioni and Tramontana, 2015), Arabia Terra (De Berardinis, 2016; Parenti et al., 2020), Tyrrhena Terra (Baioni and Tramontana, 2016), Sinus Meridiani (Baioni, 2019) and Coprates Chasma (Baioni et al., 2011). Other types of dissolution morphologies on organic materials can also be expected on Titan (Cornet et al., 2017).

In this paper, we show a remote sensing workflow to elaborate satellite images of the Pleiades constellation to perform a detailed geomorphological mapping of karst features in the salt rocks of the Cordillera de la Sal (CDS, Atacama Desert, Chile). This area was chosen for a series of reasons: (1) as other salt areas in the world, the CDS is completely devoid of vegetation (except for some areas close to the village of San Pedro de Atacama) and exhibits a typical banded terrain that has strong analogs with Martian evaporite terrains (similar to Mt. Sedom in Israel, Frumkin et al., 2021). Honeycomb and banded terrains on Mars have been explained by salt and ice diapirism, and terrestrial analogs such as Mt. Sedom and the CDS can serve to understand the processes that caused these landforms on the Red Planet (Bernhardt et al., 2016, 2019); (2) speleological explorations over the last two decades have documented a large number of dissolution caves in some restricted areas of the CDS, whereas other more remote parts are still completely unexplored. This offers the opportunity of testing the remote sensing results with bibliographic data and real ground truthing; (3) This remote sensing analysis was performed in view of a National Geographic

105 funded expedition that had the aim of exploring new caves in a previously unexplored salt area of
106 the CDS. (4) The caves actually known in the CDS are of utmost scientific importance, hosting
107 archeological findings near the village of San Pedro de Atacama, and important paleoclimatological
108 proxies (e.g., fossil bones, cave sediments, cave passage morphologies) and astrobiological targets
109 (cave mineralogy and microbiology) partially studied or still under investigation (De Waele et al.,
110 2019, 2020). Our remote sensing results have been compared and validated with a ground-truth
111 exploration of the identified entrances in two key areas of the Cordillera, Z1, a well-explored area
112 close to the village of San Pedro de Atacama, and Z7, a remote area where speleological exploration
113 never took place, and chosen as one of the main targets for the 2018 National Geographic
114 expedition (De Waele et al., 2019). Our aim was to explore the success rate of remote sensing
115 analysis in correctly identifying true cave entrances in evaporitic terrains, and to form the basis for
116 future expeditions in this extensive and extremely promising salt karst area. This methodology can
117 also work as an analogue to similar investigations in karst terrains on other planetary bodies, where
118 high resolution satellite images (HiRISE, THEMIS) and DTMs are often more readily available
119 than on Earth. The search for possible underground caves on the Moon and Mars is gaining
120 importance for many reasons: (1) caves provide access to the subsurface geology without needing to
121 drill or dig. (2) Caves on extraterrestrial bodies may host water or dry ice, brines, and organic
122 matter, (3) the underground cave temperature generally represents the average at its entrances, so
123 caves are generally warmer and more comfortable and stable environments respect to the external
124 surface. (4) Underground voids also shield possible human settlements from cosmic radiation and
125 from the often very hostile surface conditions on extraterrestrial planets. (5) For many of the above-
126 mentioned reasons caves are the most suitable locations to search for signs of present or past life
127 forms. (6) Caves are also among the best locations to establish possible future human settlements.

128

129 **2. Geological setting**

130 The Cordillera de la Sal (CDS) is located in the Central Andes (Fig.1). The Andean orogen is one of
131 the most extensive mountain belts in the world, roughly 8000 km in length and over 240 km in
132 width (Isacks, 1988; Ramos, 2009). It represents one of the most spectacular examples of an active
133 continental margin (Ramos, 2009; Rubilar et al., 2017), in which the subduction of the Nazca plate
134 below the South American plate, which started in the Lower Jurassic, is still ongoing (Isacks, 1988;
135 Ramos, 2009; Rubilar et al., 2017). The tectonic evolution of the chain has generated a complex
136 landscape characterized by rugged mountains (the highest peaks exceed 7000 m of altitude),
137 separated by sedimentary basins elongated in a roughly N-S direction (Jordan et al., 1983; Charrier
138 et al., 2007). One of these basins is the Salar de Atacama, located at the center of Atacama Desert.

139 The CDS is a NNE-SSW elongated mountain ridge that overlooks the western part of the Salar de
140 Atacama and rises above the plain for about 200 meters, representing an important structural high,
141 which exposes its rocks to considerable erosion (salt being extremely soluble). However, the hyper-
142 arid local climate (less than 20 mm/year of recorded rainfall) (Houston and Hartley, 2003; De
143 Waele et al., 2017, 2020) allowed the preservation at the surface of large volumes of extremely
144 soluble rock such as halite (NaCl). With over 22 km of salt cave passages currently verified, and
145 one of the deepest salt caves in the world (-168 m, Cueva de la Grande Quebrada) (Padovan, 2015;
146 De Waele and Padovan, 2016; De Waele et al., 2019), the CDS is a spectacular laboratory for karst
147 sciences in salt rocks (De Waele et al., 2009a, 2017).

148 The CDS is the most significant structural high of the Salar de Atacama basin, which interrupts the
149 continuity between the Llano de la Paciencia (alluvial fans outcropping to the west) and the eastern
150 area subjected to strong evaporite sedimentation (Salar). This NNE-SSW striking chain is made up
151 of a succession of Oligo-Miocene deposits belonging to the San Pedro Formation (Fm), more than
152 3000 m thick, mainly composed of sandstones, siltstones and evaporites (halite and gypsum),
153 widely deformed (Rubilar et al., 2018). In angular unconformity, the San Pedro Fm is covered by
154 Upper Miocene-Upper Pleistocene sediments corresponding to the Vilama and Campamento Fms
155 (Ramirez and Gardeweg, 1982; De Waele et al., 2020). These two units are respectively

156 outcropping in the northern and southern domains of the CDS. The Vilama Fm consists of a high-
157 frequency alternation of sandstones, pebbly sandstones, tuffs, and volcanic ashes (Upper Miocene -
158 Upper Pleistocene), whereas the Campamento Fm is composed of shales, siltstones, gypsum, and
159 halite (Pliocene - Upper Pleistocene) (Moraga et al., 1974; Rubilar et al., 2018). Following the
160 classification proposed by Becerra et al. (2014) and Henriquez et al. (2014), the San Pedro Fm is
161 subdivided into two informal units: the “Lower San Pedro Formation” (LSP) and the “Upper San
162 Pedro Formation” (USP).

163 LSP is mainly composed of halite deposits with massive fabric or apparent lamination. It presents
164 intercalations of thin layers of sandstones, siltstones, and gypsum, increasing in frequency towards
165 the top. Local intercalations of pebbly sandstones and tuffs occur in the central part of the unit. The
166 overall thickness of the salt rocks is strongly variable, generally increasing towards the north.

167 USP is constituted of a continental siliciclastic succession containing sandstones, fine
168 conglomerates, and siltstones, with intercalations of hypersaline lacustrine facies (massive halite
169 interbedded with shales and siltstones) in the upper part of the sequence.

170 Based on the distribution of different deformation styles observable along the CDS, the study area
171 can be divided into two macro-domains. The southern domain is characterized by a wide range of
172 double plunging NNE-SSW oriented anticlines and synclines, locally arranged in en-echelon
173 geometry (Wilkes and Gorler, 1988; Rubilar et al., 2018). The northern domain, on the other hand,
174 contains a series of double plunging NE-SW asymmetric anticlines and synclines, with fold cores
175 exposing the evaporitic beds of the LSP.

176 According to some authors, the deformation and the structural setting observed in the CDS could be
177 guided by mechanical stratigraphy and saline diapirism (mobile salt rocks intruding into more
178 brittle surrounding rocks), reflecting the variable evaporitic thickness from the southern to northern
179 domain (Dingman, 1962; Muñoz et al., 2002; Rubilar et al., 2018).

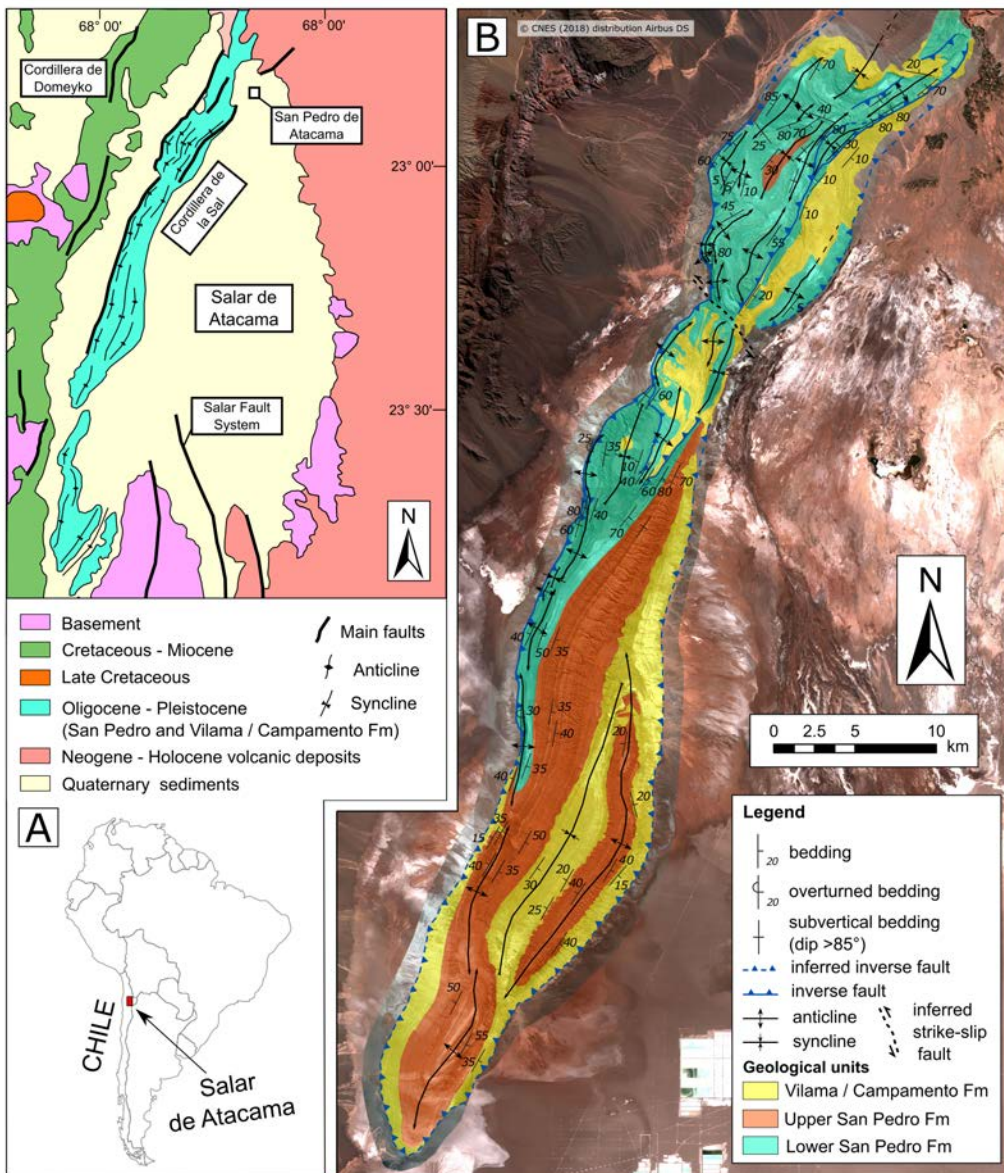


Fig. 1. A) Simplified geological map of the Atacama Desert, Chile (modified from Muñoz et al., 2002); B) geological map 1:100'000 from the Pleiades images photointerpretation of this study.

There have been several cave expeditions to the Cordillera de la Sal since the beginning of the 1990s (Salomon, 1995; Sesiano, 1998). Over the past 30 years, fifteen expeditions by French, American and Italian speleologists have led to the discovery of ca. 50 caves totaling over 22 km in length (Fryer, 2005; Sesiano, 2006, 2009; Padovan, 2015, De Waele and Padovan, 2016; De Waele et al., 2019). Most expeditions have taken place close to the San Pedro de Atacama village, where salt outcrops are easily accessible, but in the last 10 years, caves have been discovered also in the

190 central-western part of the CDS, where salt outcrops are more extensive and altitudinal gradients
191 are greater. In these last areas, the longest and deepest salt caves are located, four of which are
192 longer than 2 km, and three reach depths of over 120 meters.

193 Some caves southwest of San Pedro Village, north of the Valle de la Luna, a tourist area, have been
194 studied in detail from a geomorphological point of view because of their accessibility, great length
195 and the presence of interesting features (e.g. speleothems, sediment deposits, morphology). The
196 most important of these are the 600-m long Cueva Lechuza del Campanario (Barn Owl Cave),
197 Cueva Palacio del Sal (~ 400 m long), Cueva Paisaje Sal (660 m), and Cueva Mina Chulacao (1040
198 m long). aunal and vegetal material (bones and twigs) brought into these caves by flood events have
199 been C¹⁴-dated and, combined with Micro-Erosion Meter measurements carried out on salt surfaces
200 in external positions and in the caves, suggest speleogenesis in the Cordillera de la Sal to have
201 occurred in different climatic periods (De Waele et al., 2020). The first cave-forming episode
202 occurred during the onset of the Holocene, during which the large halite cave systems (e.g., Cueva
203 Chulacao) developed. This period of greater rainfall was followed by an early Holocene hyperarid
204 period with no cave formation, and a wetter mid-Holocene period (5-4.4 ka), during which smaller-
205 sized caves (e.g., Cueva Lechuza del Campanario) formed.

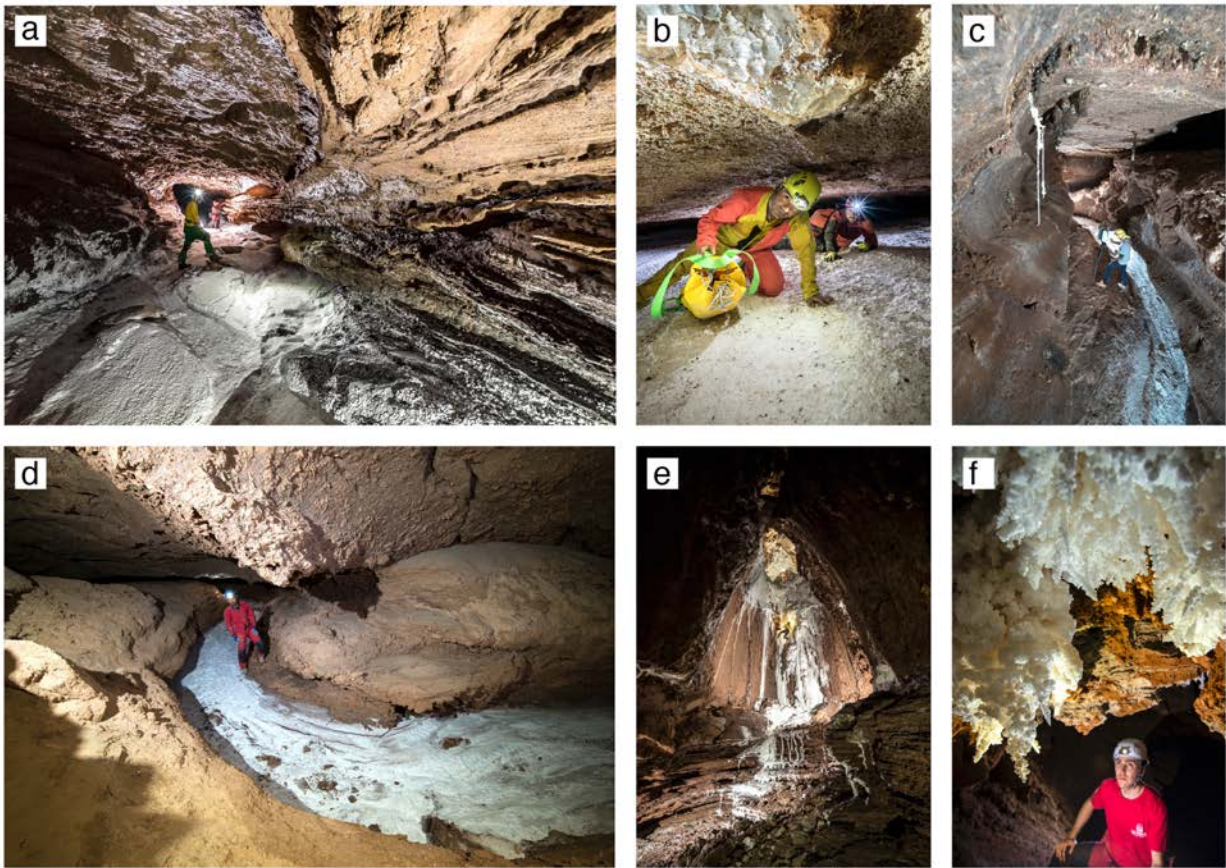
206 Most of the known caves are through-caves, with a sinking dry river bed, and an outflow toward the
207 plains (Salar to the East and Llano de la Paciencia to the West). The most important cave systems
208 are related to large drainage basins, which develop on the less permeable siliciclastic beds, in which
209 the occasional rainfall can be collected forming temporary streams able to carve the halite rock (Fig.
210 2a and c-d). In smaller drainage areas a series of small depressions can be formed (Fig.2b): the
211 alignment shows the possible presence of an underground passage, but these small features are
212 often partly filled with sediments and do not allow access to caves. Along the river beds, single
213 flood events can cause a salt bedrock retreat (dissolution) of more than 2 cm (De Waele et al.,
214 2009b). Secondary entrances can be created by the collapse of shallow underground river passages,

215 creating collapse sinkholes and skylights, generally from a meter wide to openings as great as tens
216 of meters (Fig. 2e-f).
217 Almost all caves are characteristic high underground canyons (Fig. 3c), or wide and low tubes (Fig.
218 3a-b), both with meandering morphologies (Fig. 3d) and evidence of changing base level (i.e. uplift)
219 in the form of lateral notches at various heights above the canyon floor (Fig. 3c). Especially in the
220 upstream sectors of the caves, vadose (water flowing in an air-filled underground passage)
221 entrenchment caused the formation of up to 50-m deep shafts (Fig. 3e). The currently explored salt
222 caves in the CDS have allowed the discovery of a wide variety of cave minerals (De Waele et al.,
223 2017) and speleothems (De Waele et al., 2009a; De Waele and Forti 2010) (Fig. 3f), making this
224 salt karst area one of the most interesting also from a planetary perspective, both for the abundance
225 of caves, the presence of volcanic material alongside the evaporites, and the rich mineralogy.



226
227 **Fig. 2.** Examples of cave entrances: (a) UAV photo showing the meandering canyon hosting the
228 longest salt cave in CDS (central part of Area A in Figure 7) (circles indicate persons for scale); (b)
229 Small depressions on the plateau suggesting possible cave entrances, filled with sediments or too

230 small to be entered; (c) River exiting from the vertical salt cliff at Lechuza del Campanario Cave;
231 (d) Small riverbed forming a short underground salt canyon cave in Zone 4 (see Figure 12); (e) A
232 typical shaft entrance, formed by the collapse of the roof of an underlying cave passage; (f) A
233 skylight seen from inside a cave. (Photos a, c, e, and f by Riccardo De Luca, b by Marco Mecchia,
234 and d by Alessio Romeo, La Venta Esplorazioni Geografiche).



235
236 **Fig. 3.** Salt cave morphologies: (a) Flat river passage in rock salt. Note the cemented alluvial
237 sediments on the roof, and the white salt floor; (b) Narrow and wide underground river passage; (c)
238 Laser scanner surveys in a typical high canyon with notches at different heights above the present
239 river bed; (d) Underground river meander with the white salt floor; (e) A 25 meter deep shaft in
240 halite (note caver on rope); (f) Delicate salt monocrystalline halite speleothems in a newly
241 discovered cave in Zone 3 (see Figure 12) (Photos a, b, and e, by Alessio Romeo, c by Vittorio
242 Crobu, d and f by Marco Vattano, La Venta Esplorazioni Geografiche).

244 **3. Material and methods**

245 The proposed workflow aimed to identify and map candidate cave entrances (CCEs) using satellite
246 images and a Geographic Information System (GIS). This led to the compilation of a map of CCE
247 (speleological) potential for the CDS, using an Analytical Hierarchic Process (AHP) multi-criteria
248 analysis (Saaty, 1987, 2008). The CCE potential was calculated for eight “Karst Zones”, which
249 were defined based on morpho-structural units mapped with our remote sensing investigation. The
250 zonation of morpho-structural units was performed segmenting the CDS into polygons bounded by
251 structural or stratigraphic lineaments. The CCE potential map used a multi-criteria approach,
252 combining: (i) number of unverified CCEs; (ii) coverage of salt rock outcrops; (iii) topography
253 (average elevations above the base level); (iv) cumulative length of already known caves.

254 To quantify the values for each criterion, we performed a remote sensing workflow conceptually
255 illustrated in Figure 4 and described in the following sections. Criterion (iv) obviously could not be
256 derived from remote sensing analysis and was based on pre-existing speleological literature (Fryer,
257 2005; Padovan, 2007, 2015; Sesiano, 2007). We defined this criterion basing on the assumption that
258 longer and more extensive cave systems have more chance to have larger and more abundant
259 entrances in the same area, but this is not a general rule. Therefore, a low weighting factor has been
260 chosen for this criterion (see section 3.5 for further explanation).

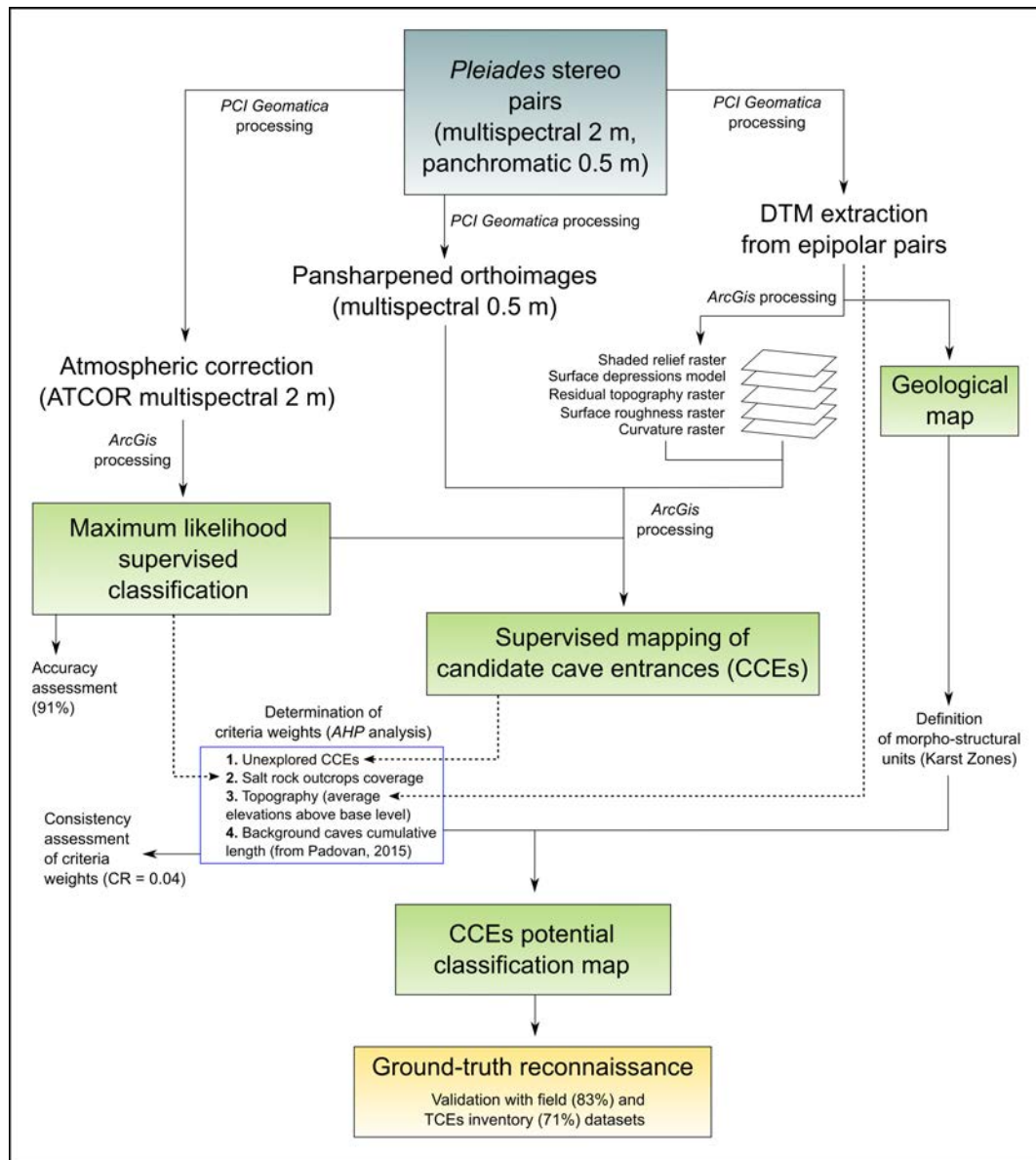


Fig.4. Schematic workflow-diagram illustrating the processing operations and analyses performed in this work.

The results of the analysis were then validated with two ground-truth datasets: a first based on a reference true caves entrances inventory dataset (TCEs), and a second based on the field validation during a National Geographic expedition in 2018 (De Waele et al., 2019).

3.1 Input data and pre-processing

270 The Pleiades images dataset was supplied by the European Space Agency (ESA). Over 600 km² of
271 Pleiades-1A and Pleiades-1B primary stereographic couples were acquired from Airbus Defense
272 and Space agency and used in this work. These satellites are part of a dual constellation system
273 capable of providing orthorectified or primary data at a spatial resolution of 0.5 m (panchromatic)
274 or 2 m (RGB and near-infrared bands).

275 For each stereo couple, one primary image was processed to obtain a raster expressed in reflectance
276 values using the ATCOR (Atmospheric Correction Ground Reflectance) tool in PCI Geomatica
277 software. Furthermore, pansharpened images (multispectral images at 0.5 m of spatial resolution)
278 were computed combining the low-resolution RGB bands with the high-resolution panchromatic
279 band using the OrthoEngine tool of PCI Geomatica (2018 version). Orthorectification operations
280 were finally performed to obtain geometrically corrected images using previously acquired
281 Sentinel-2 (level-1C) data as references for ground control points.

282 The Pleiades stereo couples were processed with OrthoEngine to manually map common
283 corresponding pixels (ground control points and tie points) and generate pairs of epipolar images.
284 Subsequently, a Semi Global Matching (SGM) algorithm was used to compute trigonometric
285 calculations basing on the geometric coefficients of the sensor and the pixels of known elevation
286 extracted from a reference 30 m-resolution DTM. Better performances in the calculation of
287 elevation values could be reached by the integration of higher quality reference DTMs or manually
288 collected GPS points. These computations were used to extract the elevation value for each cell of
289 the raster (geocoded 1 m resolution DEM). Since vegetation cover and buildings are almost
290 completely absent in the CDS, the geocoded DEMs correspond exactly to DTMs. Low-pass
291 smoothing filter (3x3 size) and noise removal adaptive Wallis filter were automatically integrated in
292 the process to eliminate outliers' pixels from the result and minimize possible sources of errors due
293 to shadows in the stereo couples (PCI Geomatica Enterprises Inc., Canada). The accuracy
294 assessment report for the SGM algorithm and DEM extraction is found in the Supplementary
295 Material section of this article.

296

297 3.2 Geological mapping

298 ATCOR corrected multispectral images were used to remotely identify areas covered by salt rock
299 outcrops. The 2 m-resolution images were displayed using a false color RGB composition as
300 follows: R (590 – 710 nm, Pleiades red band), G (430 – 550 nm, Pleiades blue band), B (740 – 940
301 nm, Pleiades near-infrared band). This preliminary visualization (Fig. 5A) helps to immediately
302 distinguish salt rock outcrops (white-grey tones) and siliciclastic lithologies (violet tones).

303 Supervised maximum likelihood classifications (Fletcher, 1987; Rossi, 2018) were used to create
304 binary maps where salt rock (soluble) and siliciclastic (insoluble) lithologies are displayed (Fig.
305 5B). These maps provide information at 2 m spatial resolution on the main areas susceptible to cave
306 formation in salt rocks.

307 DTMs and the maximum likelihood classification maps were used to calculate salt rock plateau's
308 average elevations above the base level (the Salar plains) and salt outcrops coverage (in m²), both
309 criteria involved in the AHP analysis to quantify the CCE potential.

310 Pansharpened orthoimages combined with DTMs and the above-mentioned classification maps
311 were then used for a remote-based geological mapping at 1:100'000 scale. The main stratigraphic
312 units of the study area (LSP, USP and Vilama-Campamento Fms) were mapped. ArcGis software
313 (version 10.3.1) was used to estimate measures of bedding strike and dip, calculated with simple
314 trigonometric relations extracting elevations and distances from points on the same layers (Pondrelli
315 et al., 2019). Bedding attitude permit to trace the main fold axes and produce the geological map of
316 Figure 1B.

317

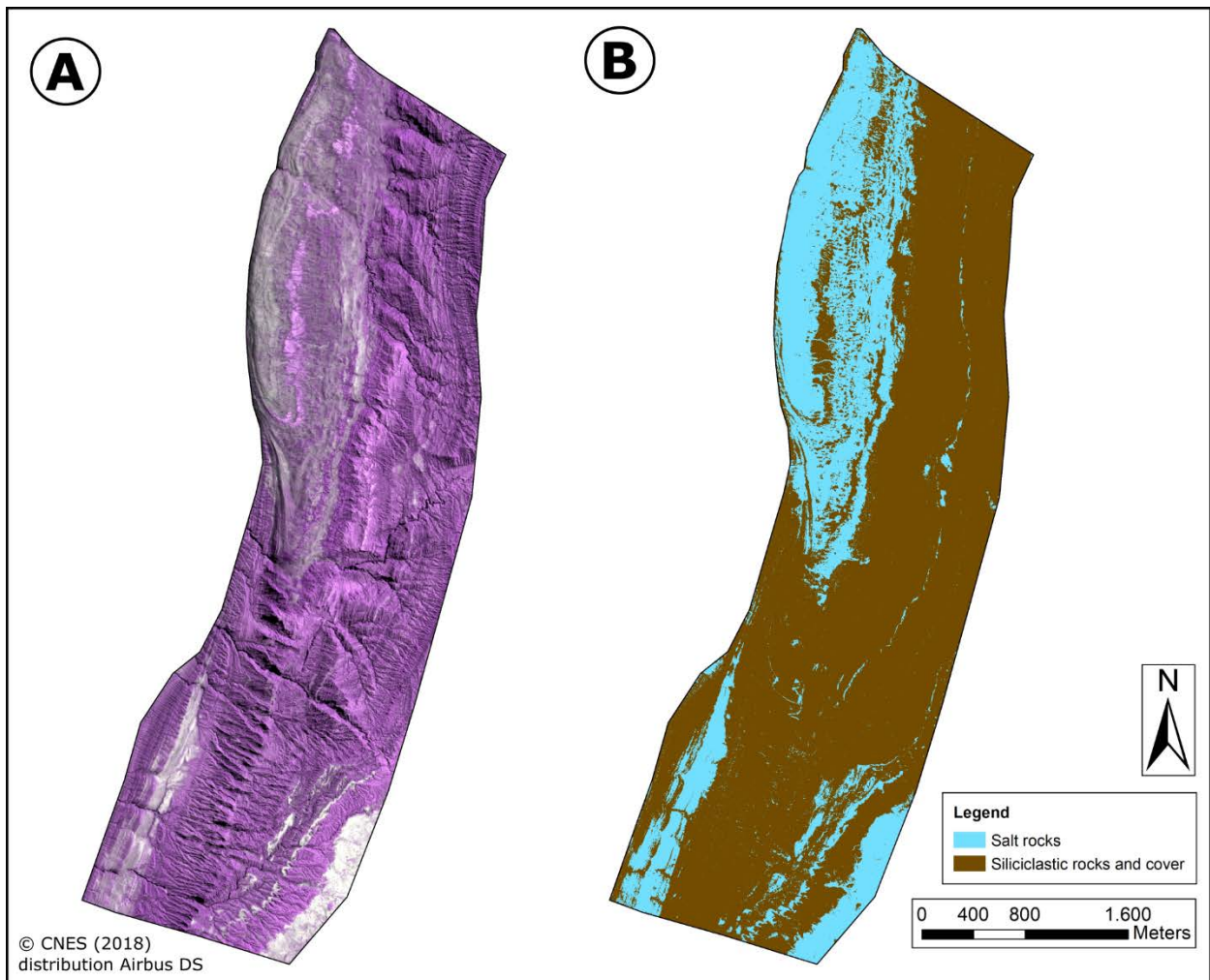
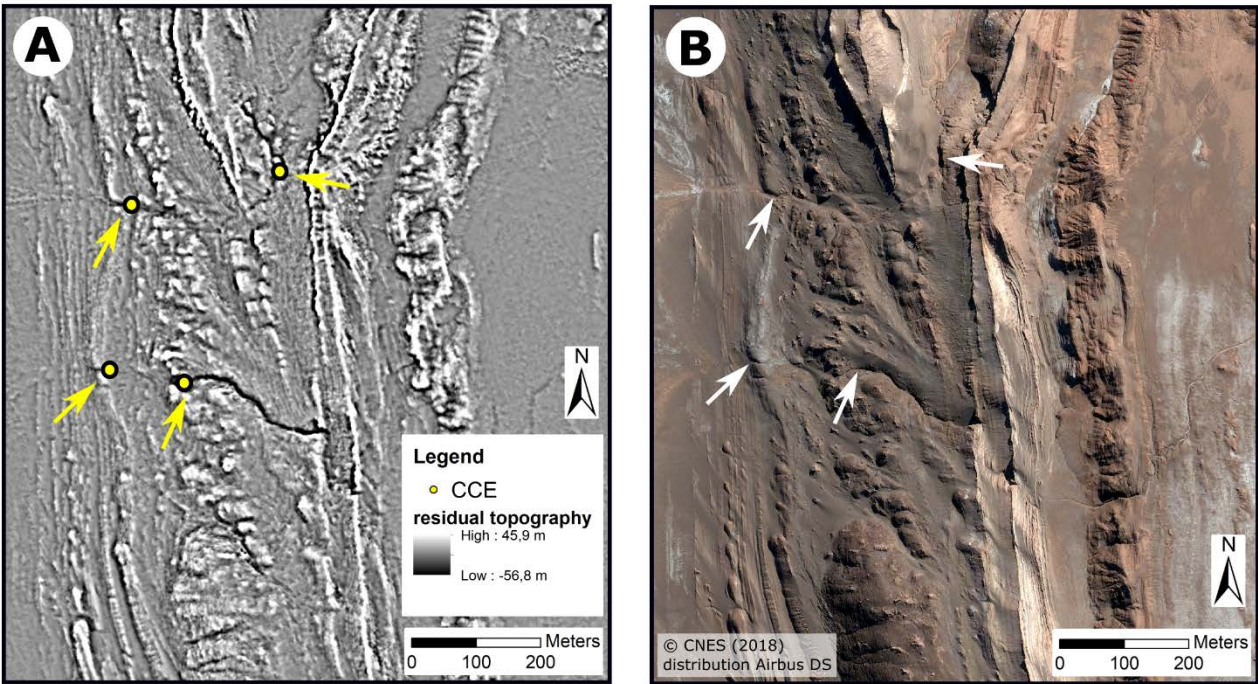


Fig. 5. A) false-color image (R: 590 – 710 nm, red band; G: 430 – 550 nm, blue band; B: 740 – 940 nm, near-infrared band) of an example area with both salt rocks and siliciclastic rocks/sediment cover; B) supervised maximum likelihood classification map of the sample area.

3.3 CCEs, TCEs and their verification

Remote sensing derived CCEs correspond to visible skylights and collapses (often large vertical openings) or interruptions of the drainage network (sinking streams or rises) (Fig.6). The identification of smaller entrances is often based on detailed morphological features, such as closed depressions or “sinking” cells. Not all these CCEs correspond to true cave entrances (TCEs), since some of these depressions might be blocked by rockfall or sediments, not allowing speleologists to enter the potentially existing underlying cave (e.g., Fig. 2b). On the other hand, some TCEs might not be visible on the satellite images for a number of reasons. For example, some meandering river

331 thalwegs (riverbeds) form deep undercuts on the convex side of the meander, therefore are hidden
332 by these overhangs from the vertical view of the satellites. Other caves are formed by dilatational
333 opening of joints in the rock, enlarged by direct rainfall and infiltration, and open on vertical walls
334 but without signs of external drainage (these caves have no sinking or rising streams). These narrow
335 openings on vertical walls can also easily be overlooked, or even be invisible, on satellite images.
336 Among the CCEs dataset, some points have been verified over the years by direct exploration from
337 cavers, to see whether or not they allow entering unexplored cave passages (defined as “Verified
338 CCEs”). The speleological exploration of salt outcrops allowed to discover a number of true cave
339 entrances (defined as “TCEs”) that represent real open passages to underground cavities, accessible
340 to humans. To estimate the quality and reliability of the CCEs dataset, the TCEs inventory has been
341 confronted with the CCEs to calculate the percentage of correctly matching points.



342
343 **Fig. 6.** Example of CCEs visualized on a DTM byproduct (residual topography raster) where
344 interruptions in drainage network are easily identified (A), and the same area on the RGB
345 pansharpened image at 0.5 m of spatial resolution (B). Note that the northernmost points were not
346 easily detectable on the original pansharpened image.

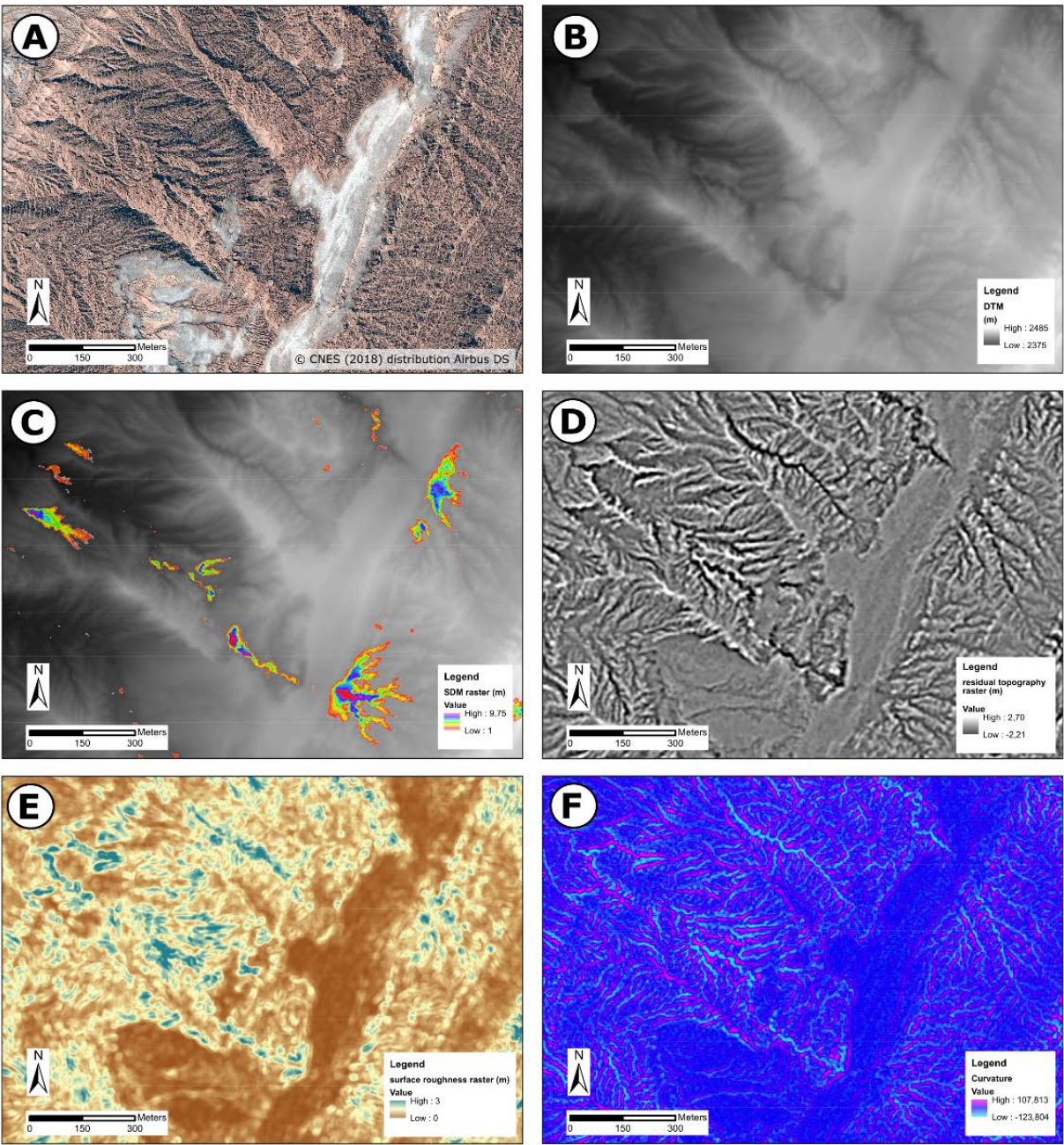
348 3.4 DTM processing and image analysis

349 Pansharpened images and DTMs were used for an image analysis workflow (performed using
350 ArcGis software) to produce a supervised mapping of CCEs. The 0.5 m spatial resolution of
351 pansharpened RGB images in the CDS allows most of these entrances to be identified with extreme
352 precision (Fig.6). However, some of the smallest features (< 1 m in diameter) could remain
353 undetected. To improve the geomorphological mapping, the 1 m resolution DTMs were processed
354 to highlight: surface depressions (sinkholes, collapses), topographic variability (canyons, streams,
355 and reliefs), surface roughness, and terrain curvature (Fig. 7).

356 The first phase of DTM processing led to the creation of “shaded relief” rasters, extracted using the
357 “hillshade” tool in ArcGis and applying a mono-directional illumination source and angle.
358 Hillshade models are valuable and immediate tools to enhance morphological features and
359 landscape morphologies. Multi-directional shading techniques, although not used in our analysis,
360 may minimize errors due to shadowed areas. Subsequently, we compiled “surface depression
361 models” (SDM), which are rasters calculated by the difference of the filtered DTMs (where sinking
362 cells in the surficial drainage are filled with the ArcGis “fill” tool) and the original non-filtered
363 DTMs. These models highlight closed-drainage cells (sinkholes, collapses, skylights) and sinking
364 streams where the surface drainage is interrupted.

365 “Residual topography” rasters were compiled as the difference of original DTMs and normalized
366 DTMs where cell values are expressed as the mean values of a 10x10 m rectangular window
367 centered on each cell. This raster provides an excellent indicator of linear geomorphic features such
368 as canyons, valleys, and streams (negative values), and topographic highs (positive values). Indices
369 of “surface roughness” were also compiled, visualized with a raster where each cell has a value of
370 standard deviation calculated in the 10x10 m rectangular window from each cell of the “residual
371 topography” raster. “Surface roughness” provides an important contribution to understand the
372 morphological variability and topography of the examined area, as it allows to measure the local
373 variability of elevations at a scale of few meters with such detailed DTMs (Haneberg et al., 2005;

374 Cavalli and Marchi, 2008). Finally, terrain curvature rasters (Cavalli et al., 2013; Nonomura et al.,
 375 2019) were extracted from the DTMs using the “curvature” tool in ArcGis. Curvature is defined as
 376 the rate of change of the slope and is usually determined as the second derivative of the surface.
 377 Curvature values provide a measure of convergency or divergency of flow and, together with
 378 “residual topography” rasters, can be used to identify raw drainage networks (Cavalli et al., 2013).



379
 380 **Fig. 7.** Example of the selection of rasters used for the geomorphological mapping of CCEs in an
 381 example area. A) pan-sharpened RGB image; B) 1 m resolution DTM; C) surface depressions model

382 (SDM) extracted using the difference of a holes-filtered DTM and the original one; D) residual
383 topography raster, with negative values (black to dark grey) corresponding to canyons, streams and
384 valleys; positive values (light grey to white) indicate prominent reliefs, scarps, crests; E) surface
385 roughness raster, useful to discriminate different types of terrains and canyons; F) curvature raster
386 which is a reflection of convergency-divergency of the surface drainage pattern.

387

388 3.5 AHP analysis and CCE (speleological) potential map

389 The Analytic Hierarchy Process (AHP), introduced by Thomas Saaty (1980), is an effective tool for
390 dealing with complex decision-making and ranking classifications. AHP is used to quantify weights
391 for each evaluation criteria involved in the analysis, which is determined after pairwise comparisons
392 among the different criteria supervised by the user. In addition, the AHP incorporates a valuable
393 technique for checking the consistency of the decision maker's pairwise comparisons, thus reducing
394 the bias in the decision-making process.

395 In order to compute the weights for the different criteria, the AHP starts creating a pairwise
396 comparison matrix. The pairwise comparison matrix is a $n \times n$ real matrix, where n is the number
397 of evaluation criteria. Each cell a_{ij} of the matrix represents the importance of the i criterion
398 relatively to the j criterion. If $a_{ij} > 1$, the i criterion is more important than the j criterion (and vice
399 versa). Values attributed to the cells are evaluated following the reference values reported in in
400 Table 1. Furthermore, the entries a_{ij} and a_{ji} must satisfy the following equation:

$$401 \quad a_{ij} \cdot a_{ji} = 1$$

402 The weights vector w (a n -dimensional columnar vector) is thus calculated from the following
403 equation, where \bar{a}_{ij} are the normalized values of the pairwise comparison matrix:

$$404 \quad w_i = \frac{\sum_{j=1}^n \bar{a}_{ij}}{n}$$

405

406 **Table 1.** Scale used to attribute the relative importance in the pairwise comparison matrix (from
 407 Saaty, 1980).

Relative importance	Definition	Explanation
1	Equal importance	The two criteria contribute equally
3	Weak importance	Experience and judgment slightly favor one criterion over the other
5	Strong importance	Experience and judgment strongly favor one criterion over the other
	Demonstrated	
7	importance	One criterion is strongly favored and demonstrated in practice
	Extreme	The evidence favoring one criterion over the other is of highest
9	importance	possible order of affirmation
	Intermediate	When compromise is needed between two adjacent relative
2, 4, 6, 8	importance	importance values

408

409 The consistency ratio (*CR*) of the AHP is calculated to evaluate the statistical consistency of the

410 pairwise comparisons and for detecting contradictions in the attribution of criteria’s relative

411 importance. The *CR* value is calculated as the ratio between the consistency index (*CI*) and the

412 random consistency index (*RI*) as proposed by Saaty (1980):

413
$$CR = \frac{CI}{RI}$$

414 Where:

415
$$CI = \frac{\lambda_{max} - n}{n - 1}$$

416
$$\lambda_{max} = \text{Principal eigenvalue}$$

417 *RI* depends on the number of criteria (*n*) as proposed by Saaty (1980) in Table 2. The pairwise

418 comparison matrix is considered statistically consistent when *CR* < 0.1. The *CR* value for our AHP

419 analysis is equal to 0.04 and is therefore considered acceptable.

420

421 **Table 2.** Random consistency index (from Saaty, 1980).

<i>n</i>	1	2	3	4	5	6	7	8	9	10	11	12
RI	0	0	0,58	0,9	1,12	1,24	1,32	1,41	1,45	1,49	1,51	1,53

422

423 The pairwise comparison matrix and relative calculated weight for each criterion is displayed in
424 Table 3. The calculated weights have values ranging from 0 to 1, with 0 corresponding to the lowest
425 importance and 1 to the highest. For each Karst Zone, we computed a cumulative weighted score
426 (*CS*) combining the weight vector (*w*) and the normalized values (*v*) attributed to each criterion:

427
$$CS = v \cdot w$$

428 The final scores were then classified using Jenks natural breaks optimization (Jenks, 1967) into four
429 classes: low, medium, high, and very high CCE (speleological) potential.

430

431 **Table 3.** Pairwise comparisons matrix and weights calculated for each evaluation criterion. Criteria:
432 1) number of unverified CCEs; 2) coverage of salt rock outcrops; 3) topography (average elevations
433 above the base level); 4) cumulative length of already known caves (based on previous literature
434 data).

PAIRWISE COMPARISON MATRIX

criteria	1	2	3	4	calculated weights
1	1	2	4	7	0,50
2	1/2	1	2	6	0,28
3	1/4	1/2	1	5	0,17
4	1/7	1/6	1/5	1	0,05

435

436 **4. Results**

437 4.1. CCEs mapping and morpho-structural segmentation

438 Using the geological map (limits of the lithostratigraphic units) and the main structural lineaments
439 (faults and folds), we segmented the CDS into eight morpho-structural units, called Karst Zones,
440 from Z1 to Z8 (Fig.8). A short description of each is given below.

441 Z1 hosts the northernmost NE-SW oriented folds exposed in the CDS and located south of the
442 village of San Pedro de Atacama. This area is covered by the northern portion of the “Valle de la
443 Luna Natural Park”, and was easily accessible until 10 years ago, before stricter Park rules were set
444 in place. The area comprises a steeply inclined NE-SW oriented anticline where the highest number
445 of CCEs has been explored so far (Quebrada Honda anticline), with over 3 km of mapped cave
446 passages (Fryer, 2005; Padovan, 2015). In total, 32 CCEs were mapped, 11 of which have never
447 been field-checked.

448 Z2 is covered by the southern portion of “Valle de la Luna Natural Park” and comprises a complex
449 architecture of NE-SW oriented asymmetric anticlines and synclines bounded by inverse faults. In
450 this area of difficult access, a surprisingly small number of caves has been explored (~ 600 m of
451 mapped cave passages). In total, 30 CCEs were mapped, 7 of which were verified and gave access
452 to caves. Note this area contains 24 TCEs, meaning that many cave entrances (17), which give
453 access to relatively small caves, are not visible on satellite images (Sesiano, 2007).

454 Z3 is located immediately south of Z2, and is characterized by asymmetric and inclined NE-SW
455 oriented folds, with a lower amount of shortening respect to Z2. Its southern limit is an inferred sub-
456 vertical strike-slip fault zone marking the transition with the southern tectonic domain of the CDS.
457 In this area, entirely lacking access routes, no speleological explorations were carried out so far. In
458 total, 27 CCEs were mapped.

459 Z4 is characterized by NNE-SSW oriented asymmetric folds. This unit is at the transition between
460 the northern and southern domain of the CDS. Inverse faults mark the lateral limits with Z5. The
461 longest explored cave system of CDS is found in this area (Dario Cressi Cave System, more than 5
462 km long; Padovan, 2015). In total, 38 CCEs were mapped, 11 of which gave access to often large
463 underground passages, the remainder not having been checked in the field.

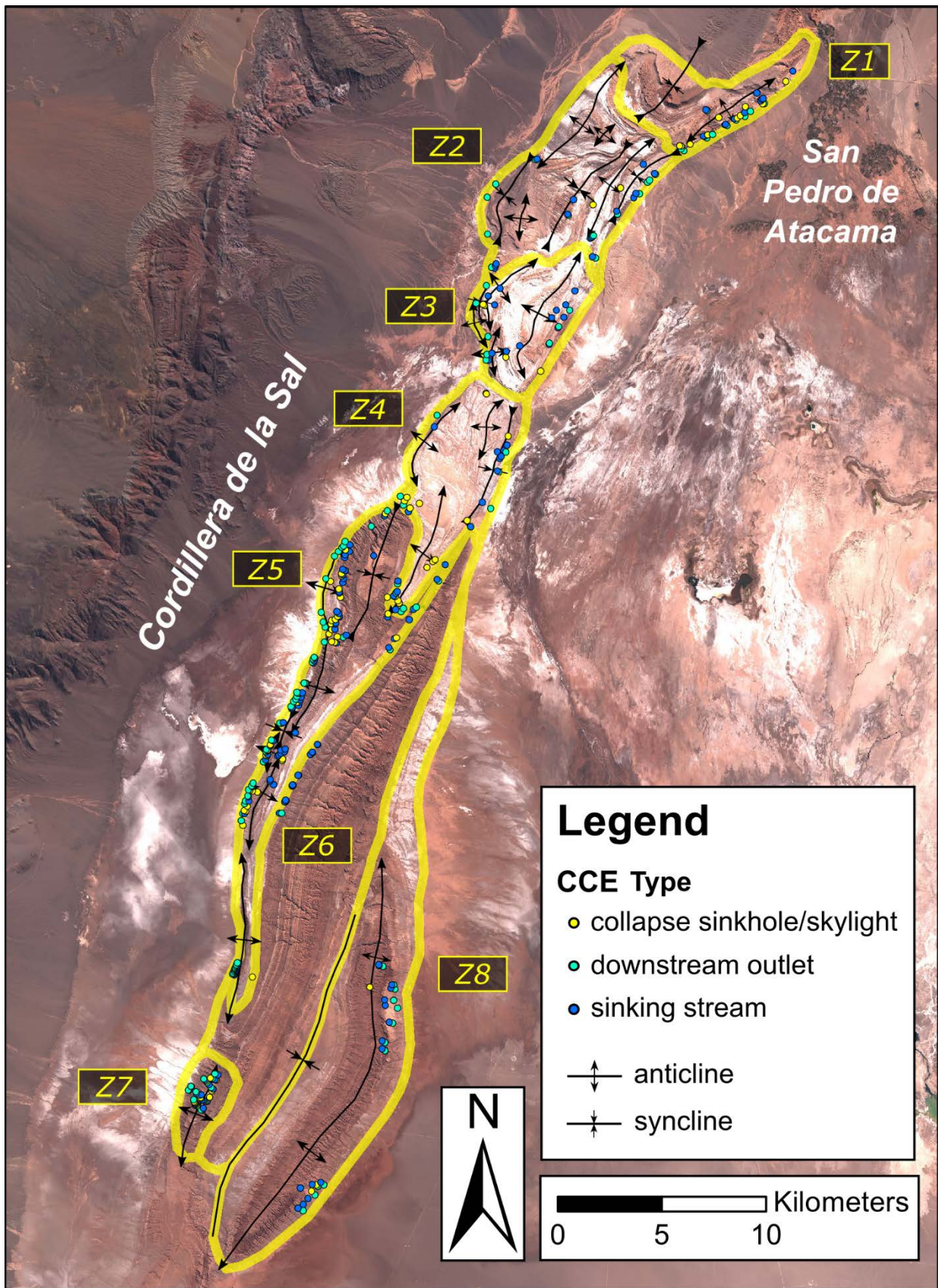
464 Z5 comprises an elongated area at the western front of the chain where a series of NNE-SSW west-
465 vergent asymmetric anticlines (occasionally overturned) outcrop. The lateral limit with Z6
466 corresponds to the lithostratigraphic contact between LSP and USP Fm. This area hosts the highest
467 number of explored caves (more than 9 km of mapped cave passages) and the deepest cave system
468 of the CDS (168 m of total depth). In total, 153 CCEs were mapped, but only 27 points were
469 verified by Italian cavers giving access to important and long cave systems (Padovan, 2015).

470 Z6 comprises the ESE-dipping limbs of the main folds outcropping in Z5. This area also hosts the
471 lowest number of CCEs (20) and the smallest areas with outcropping salt rocks, given that it is
472 entirely covered by the USP and Campamento Fms. The southeastern limit with Z8 corresponds to
473 a main syncline axial trace. This area is still completely unexplored.

474 Z7 is characterized by an isolated NNE-SSW anticline exposing an extensive salt rock core in its
475 northern part. In this salt rock core, 41 CCEs were mapped, none of which was reached before our
476 2018 expedition. We verified 28 of these entrances, 24 of which proved to be TCEs.

477 Z8 comprises the main NNE-SSW elongated symmetric anticline composed of USP Fm at the
478 southeastern margin of CDS. The lateral limit with Z6 corresponds to a main syncline axial trace (in
479 the southern part) and the lithostratigraphic contact between USP and Campamento Fms (in the
480 northern part). CCEs in this area (30) were found predominantly in the salt rock beds of
481 Campamento Fm and have never been object of speleological expeditions before 2018. We were
482 able to reach 7 out of these, 5 of which gave access to caves.

483 The general attributes extracted for the eight Karst Zones are summarized in Table 4. In each Karst
484 Zone, mapped CCEs were attributed to three types (sinking streams, collapse sinkholes-skylights,
485 downstream outlets) and the hosting lithology (Fig.9). The global table with all the 371 CCEs points
486 is included in the Supplementary Material of this article.



487

488 **Figure 8.** Segmentation in morpho-structural units and mapped CCEs. Base map: Sentinel-2 image

489 (S2A_MSIL1C_20170519T143751_N0205_R096_T19KEQ_20170519T143812).

490

491 **Table 4.** Summary of the Karst Zones attributes.

Karst Zones	Stratigraphic units	Area (km ²)	Salt Coverage (%)	min/max			
				Elevation (m a.s.l.)	CCEs	TCEs	Verified CCEs
Z1	LSP Fm, Vilama Fm	27,18	13	2459/2715	32	26 ^a	21
Z2	LSP Fm, USP Fm	50,73	37	2436/2675	30	24 ^b	7
Z3	LSP Fm, Vilama Fm	26,41	32	2389/2671	27	/	0
Z4	LSP Fm, Vilama- Campamento Fm	35,82	47	2366/2675	38	13 ^c	11
Z5	LSP Fm, Campamento Fm	54,39	33	2370/2695	153	25 ^c	27
Z6	USP Fm, Campamento Fm	110,23	6	2350/2654	20	/	0
Z7	USP Fm	9,48	13	2375/2485	41	24 ^d	28
Z8	USP Fm, Campamento Fm	97,61	8	2308/2452	30	5 ^d	7

492 ^a from caves reported in Padovan (2007, 2015) and Fryer (2005); ^b 7 cave entrances mapped by
493 French teams (Sesiano, 2007) and 17 entrances from the cave register of Fryer (2005) and Padovan
494 (2007, 2015); ^c based on Padovan (2015); ^d from the 2018 exploration, De Waele et al. (2019).

495

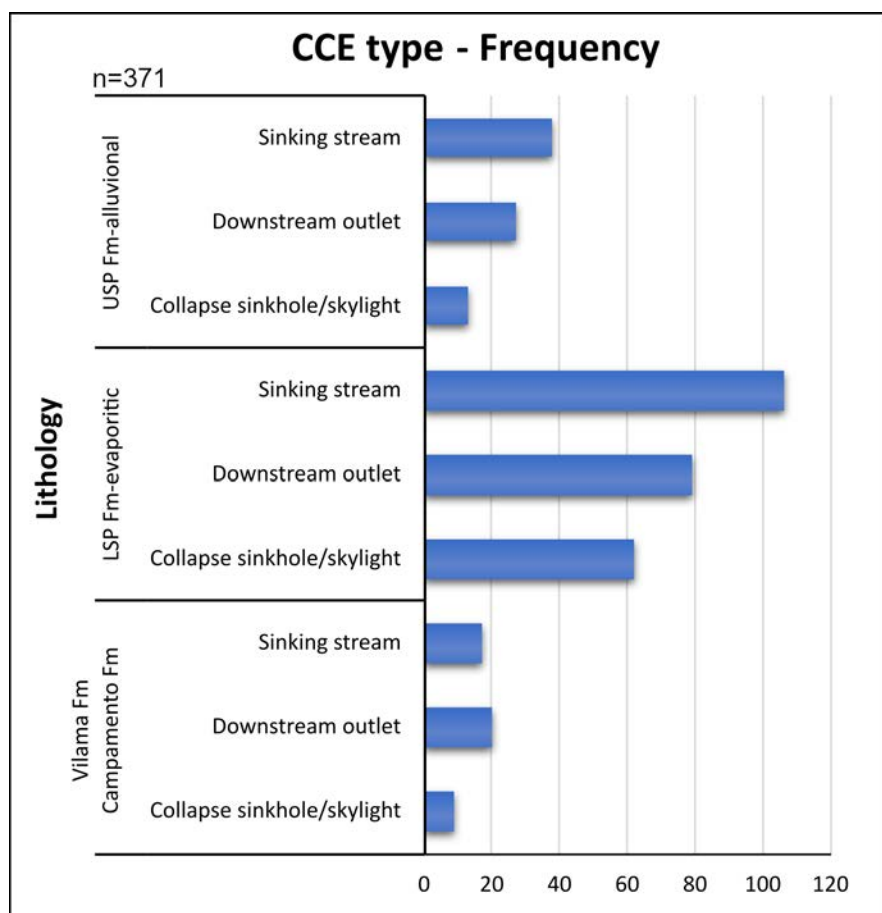


Figure 9. Frequency of the CCEs divided by lithology and type.

4.2. Evaluation of the karst zones CCE potential

The evaluation of the CCE potential was carried out using the data available on caves and cave entrances prior to our 2018 National Geographic funded expedition (De Waele et al., 2019). This analysis was part of our preparatory work for the expedition and allowed us to have great exploration results (almost 3 km of newly explored caves).

The results of the cumulative weighted scores of the AHP analysis for each Karst Zone are displayed in Table 5, and classified with Jenks natural breaks optimization to produce a CCE potential map of the CDS (Fig.10). The limits between the different classes are: low (0; 0.071), medium (0.071; 0.10), high (0.10; 0.15) and very high (0.15; 0.33).

Two units (Z1 and Z6) were classified in the “low potential” class; three units (Z3, Z7 and Z8) in the “medium potential” class; two units (Z2 and Z4) in the “high potential” class and one unit (Z5) in the “very high potential” class.

After the analysis, the southernmost morpho-structural units (Z7 and Z8) with medium CCE potential and where no speleological research was performed, were selected to be the main objective of the National Geographic funded field expedition (De Waele et al., 2019).

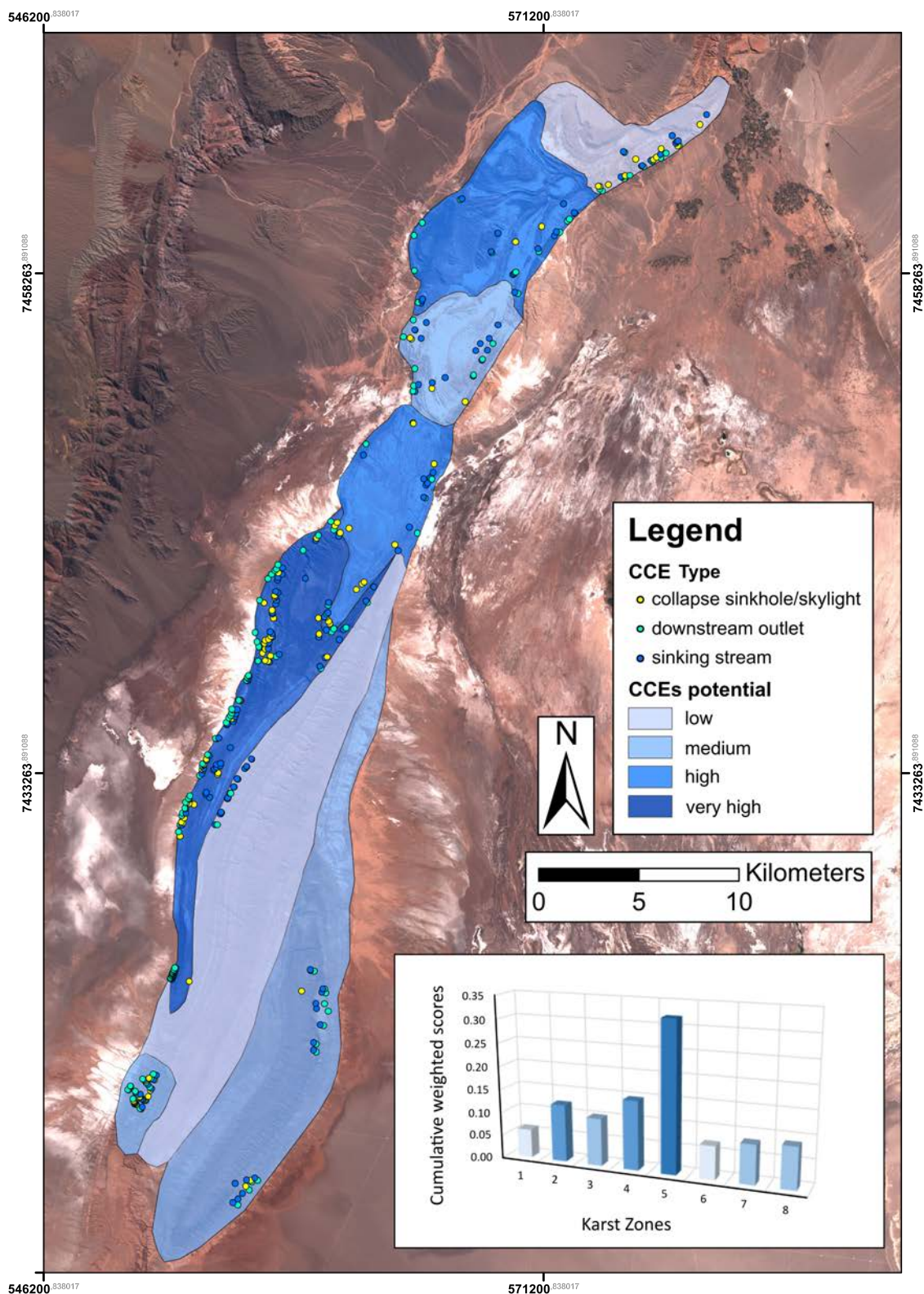
Table 5. AHP analysis and cumulative weighted scores for the eight identified Karst Zones.

Salt				
Karst	Unverified	coverage	Average elevation above	Background caves
Zone	CCEs (n)	(m ²)	base level (m)	total length (m)
Values				
1	11	3648132	117	3684
2	23	18901196	101	606
3	27	8550570	155	0
4	27	16768758	182	5361
5	126	17854817	191	9390
6	20	6443559	90	0
7*	41	1195602	63	0
8*	30	8052424	64	0
sum	305	81415058	963	19041
weights	0,50	0,28	0,17	0,05
Normalized values				
1	0,04	0,04	0,12	0,19
2	0,08	0,23	0,10	0,03

3	0,09	0,11	0,16	0,00
4	0,09	0,21	0,19	0,28
5	0,41	0,22	0,20	0,49
6	0,07	0,08	0,09	0,00
7	0,13	0,01	0,07	0,00
8	0,10	0,10	0,07	0,00
<i>sum</i>	<i>1,00</i>	<i>1,00</i>	<i>1,00</i>	<i>1,00</i>

<i>Weighted scores</i>					<i>Cumulative</i>
					<i>weighted scores</i>
1	0,018	0,013	0,021	0,010	0,06
2	0,038	0,065	0,018	0,002	0,12
3	0,044	0,029	0,027	0,000	0,10
4	0,044	0,058	0,032	0,014	0,15
5	0,207	0,061	0,034	0,025	0,33
6	0,033	0,022	0,016	0,000	0,07
7	0,067	0,004	0,011	0,000	0,08
8	0,049	0,028	0,011	0,000	0,09

516 * this analysis does not include the new caves explored in Karst Zones 7 and 8 during the National
517 Geographic expedition of 2018 (De Waele et al., 2019).



518

519 **Fig. 10.** CCE (speleological) potential map of the CDS morpho-structural units, with mapped
 520 CCEs. The cumulative weighted scores obtained with the AHP analysis are also displayed with a
 521 diagram. Base map: Sentinel-2 image
 522 (S2A_MSIL1C_20170519T143751_N0205_R096_T19KEQ_20170519T143812).

523
524
525
526
527
528
529
530
531
532
533
534
535
536
537
538
539
540
541
542
543
544

4.3. Ground-truthing

To validate the remote-sensing classification of salt rocks (Fig.5) a confusion matrix was computed combining 96 ground-truth control points (GCP) in which lithology was observed directly on the field, enabling the evaluation of the reliability of the maximum likelihood classification maps (Table 6). The global accuracy of the image classification was 91%, with the “salt rocks” class correctly covering 98% of the total ground truth points of the same category.

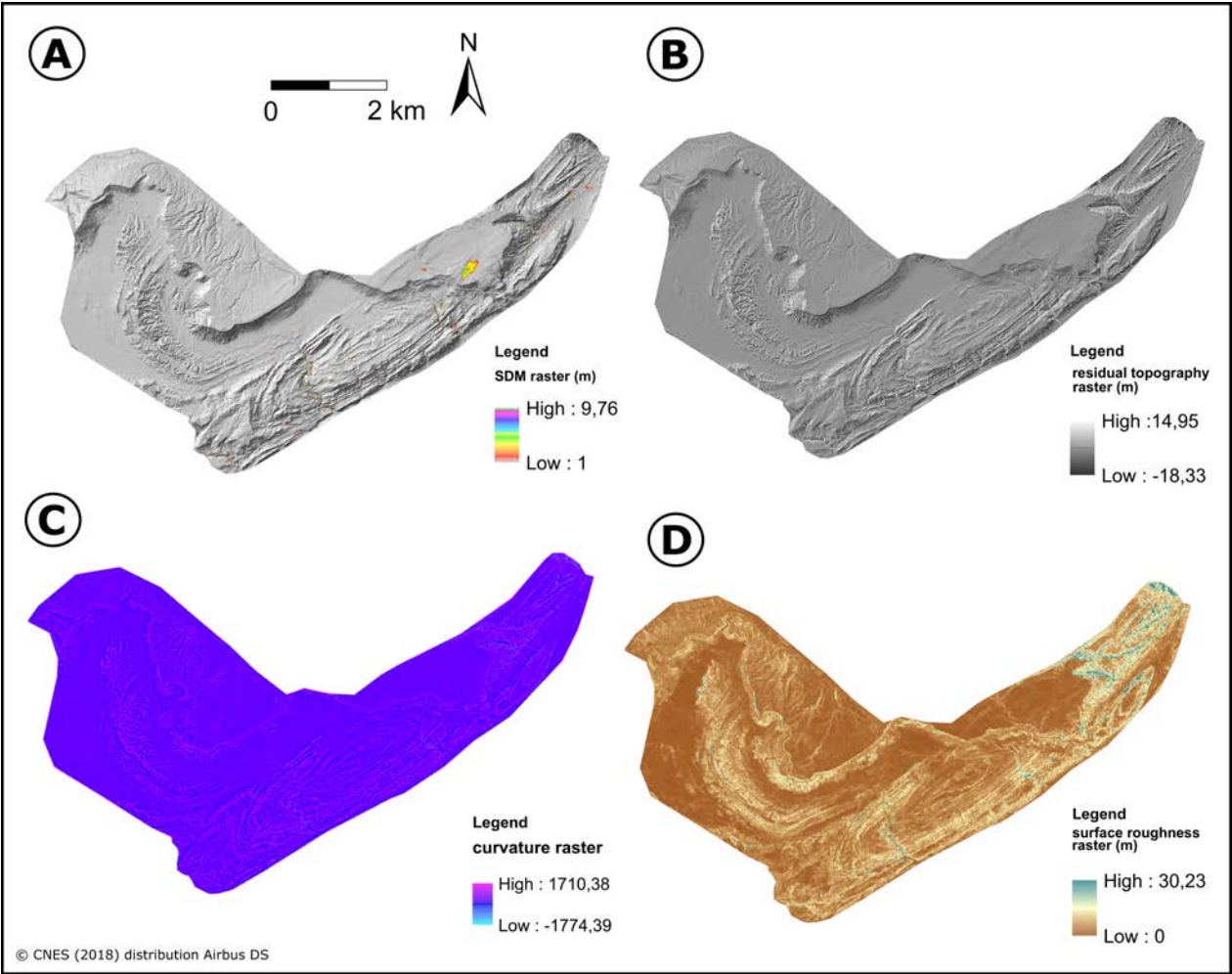
Table 6. Confusion matrix for the maximum likelihood classification analysis and accuracy assessment of lithological mapping through remote sensing.

Class	GCP 1 (salt rocks) n=52	GCP 2 (siliciclastic rocks) n=44	Percentage
Salt rocks	44	1	98%
Siliciclastic rocks	8	43	84%
Global accuracy			91%

Two sample study areas were selected to visualize the results obtained by remote sensing and the ground-truth validation of cave entrances. The selected areas were chosen among the eight morpho-structural units and correspond to Z1 and Z7 (Fig.8). The northern one (Z1) is the area with the lowest degree of unexplored CCEs (11, corresponding to 34%), in which explorations for caves has been carried out in earlier expeditions (Salomon, 1995; Sesiano, 1998; Fryer, 2005; Sesiano, 2006, 2009; Padovan, 2015, De Waele and Padovan, 2016). The southern area (Z7) on the contrary, was completely unexplored before our 2018 expedition. Therefore, the remote sensing results obtained for Z7 unit were useful for the organization of a true caving expedition, and the most promising CCEs were directly verified on the field.

Rasters extracted from the DTM processing of the two areas are displayed in Figures 11 and 13, respectively. The CCEs were subdivided in three types (sinking streams, sinkholes/skylights, and

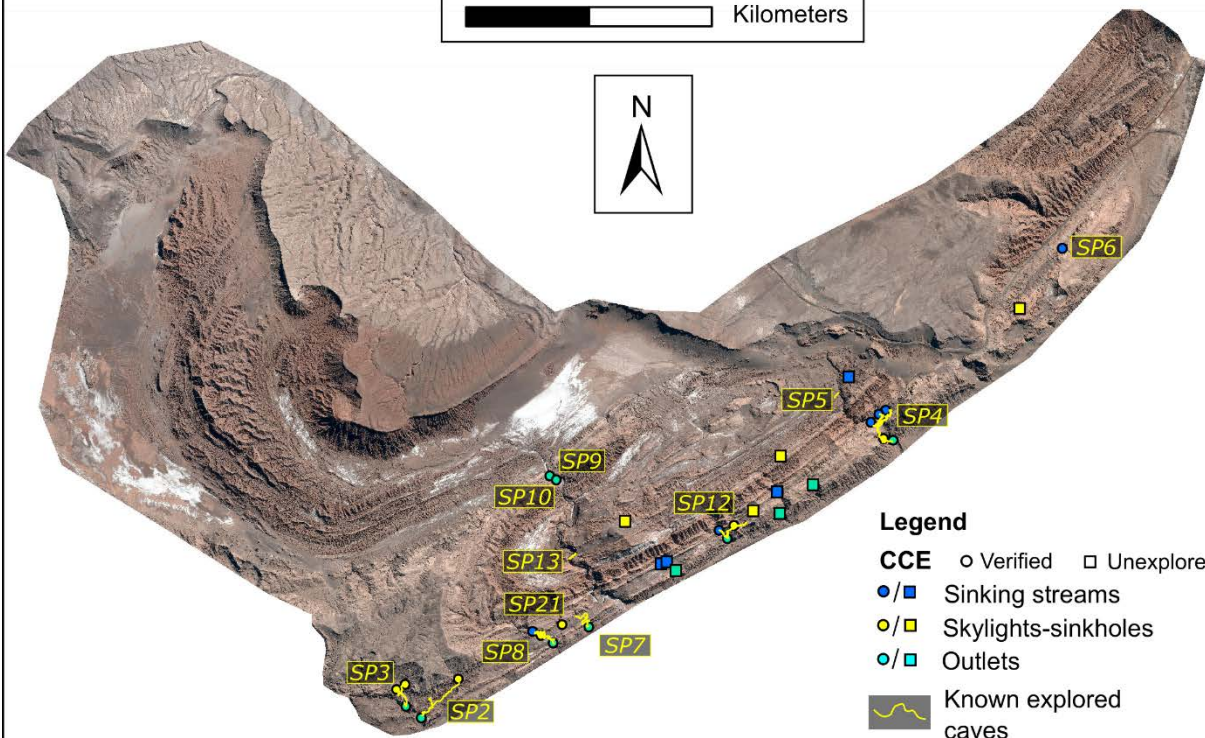
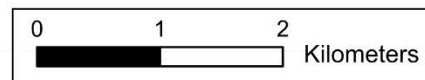
545 downstream outlets), by degree of knowledge (verified or unexplored), and displayed in maps with
546 the pansharpened ortho-images as base rasters (Figs. 12 and 14). The figures also show the
547 underground traces of the verified and known caves.
548 In the Z1 unit (Fig. 12), we had the possibility to test the analysis with an already existing cave
549 inventory: within the 26 TCEs explored up to date, 21 CCEs were correctly matching, whereas 5
550 TCEs were not corresponding to our CCE dataset.



551
552 **Fig. 11.** Results obtained for the Z1 unit (Fig.8); A) SDM raster overprinted on shaded relief raster;
553 B) residual topography raster; C) curvature raster; D) surface roughness.

Z1

© CNES (2018) distribution Airbus DS

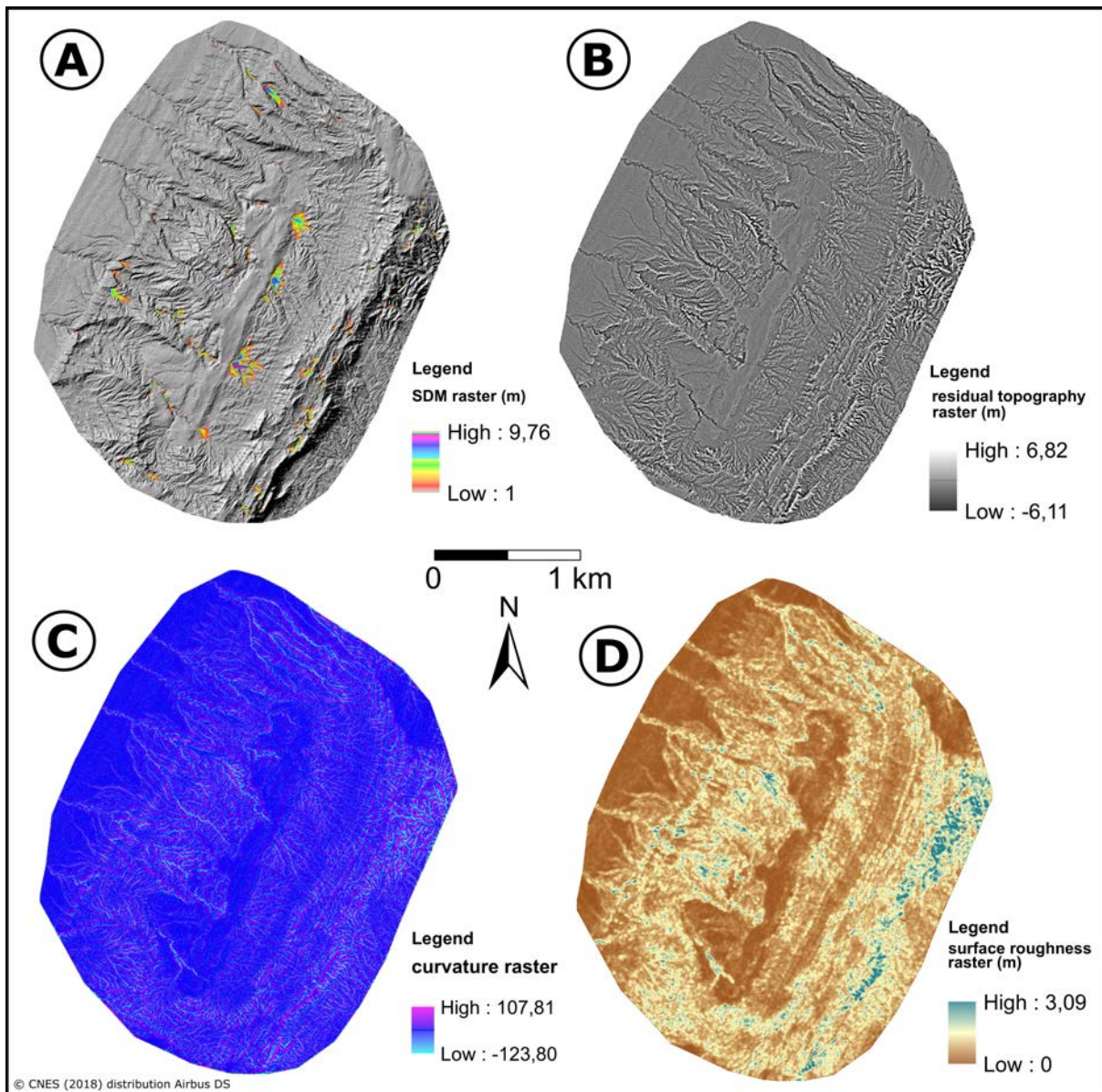


554

555 **Fig. 12.** Pansharpened orthoimage of the Z1 unit, with the mapped CCEs and known cave
 556 planimetries (cave labels are extracted from the inventory of CDS by Padovan, 2015).

557

558 In the Z7 unit (Fig.14), many points selected as CCEs (corresponding to 68% of the total) were
 559 reached and verified during the 2018 expedition. Among the 28 verified CCEs, 24 corresponded to
 560 TCEs leading to a real accessible subterranean void. However, 4 CCEs in salt rocks did not match
 561 with true cave entrances, and 13 (less promising) CCEs are still unexplored after the 2018
 562 expedition (not reached because of time constraints and terrain difficulties).



563

564 **Fig. 13.** Results obtained for the Z7 unit (Fig.8); A) SDM raster overprinted on shaded relief raster;

565 B) residual topography raster; C) curvature raster; D) surface roughness.

Z7

© CNES (2018) distribution Airbus DS

Small
cave passages

Legend

CCE ○ Verified □ Unexplored

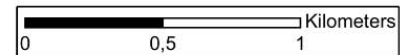
●/■ Sinking streams

●/■ Skylights-sinkholes

●/■ Outlets

Known explored caves

1. Cueva Primero Sal 1
2. Cueva Primero Sal 2
3. Cueva Apollo 1
4. Cueva Apollo 2
5. Cueva Apollo 3
6. Cueva Agujas
7. Cueva Dama del Quiosco



566

567 **Fig. 14.** Pansharpened orthoimage of the Z7 unit, with the mapped CCEs and known caves
568 planimetries.

569 In a similar way, a confusion matrix between the CCEs and TCEs datasets were calculated for all
570 the Karst Zones, distinguishing from the true caves inventory verification (for Z1, Z2, Z4, and Z5)
571 and the field-based verification in completely unexplored areas (for Z7 and Z8) (Table 7). The
572 results show a global average success rate of 76%. A measure of the accuracy of the remote-sensing
573 derived CCEs in finding new accessible cave systems is represented by the field-based validation
574 method (zones Z7 and Z8), with an average accuracy of 83% (29 out of the 35 verified CCEs lead
575 to true cave entrances).

576

577 5. Discussion and conclusions

578 The complete absence of vegetation and human settlements (excluding the San Pedro Village and
579 the few dirt roads along the borders of the Cordillera) and the outcropping soluble rocks make the
580 CDS a perfect analogue of possible extraterrestrial evaporite karst areas (Baioni et al., 2009).

581 Contrary to the generally large collapse entrances of lava tubes, halite cave entrances can be rather
582 small (even less than half a meter wide) and can also be located at the foot of small cliffs, under
583 overhanging walls, making them invisible in most satellite images with a zenithal view. The CDS
584 combines a series of characteristics which make it an ideal analogue site to verify the accuracy of
585 remote sensing in the mapping of candidate cave entrances (CCEs), which are: 1) it has a large size
586 (over 80 km long and up to 8 km wide), greater than most diapirs (e.g., Iran, Bosák et al., 1999); 2)
587 some areas of the CDS are rather well explored in respect to other salt areas in the world (only Mt.
588 Sedom in Israel has been investigated more in detail, e.g., Frumkin, 1998) with a good database of
589 over 50 mapped caves, corresponding to ~22 km of underground passages, useful to make
590 comparisons between remote-sensing derived data and ground-truthed caves; 3) large areas remain
591 completely unexplored, and the CCEs can be checked in the field to verify how well the cave
592 prediction method performs.

593 Based on the results obtained during our remote sensing workflow, 371 CCEs have been identified.
594 Most of the mapped CCEs are located in the LSP Fm, as expected, being almost entirely
595 represented by thick halite beds. The LSP and Vilama/Campamento Fms, on the other hand, show a
596 lower number of entrances (Fig.9). In the San Pedro Fm, the most frequent types of entrances are
597 sinking points of ephemeral streams where they contact the inclined salt rock beds on the flanks of
598 the main outcropping folds (see example in Fig.12). These kinds of entrances resulted to be the
599 easiest for identification and mapping using our image analysis workflow. The collapses/skylights
600 type, on the other hand, is the less represented class. This reflects the fact that most of these
601 entrances are collapses directly putting in connection the overlying siliciclastic sediments to
602 underlying cave passages in salt rock beds, with poor or inexistent relation with the drainage
603 network (Fig.7). In addition, these collapses can also be relatively small, below the DTM resolution.

604 In almost all the four lithostratigraphic units, sinking streams have a slightly higher frequency in
605 respect to downstream outlets, proving that most of the base-level outlets of the meandering cave
606 passages could be undetected due to sediment fillings or less prominent topographic signatures on
607 DTM by-products (Fig.6).

608 To evaluate the global accuracy of our analysis, our large dataset was tested with two different
609 methods: i) comparing it to a literature-derived reference TCEs dataset, and ii) comparing it to a
610 field-based validation during 2018 expedition. The global correspondence table between CCEs,
611 TCEs and verified CCEs after ground-truthing is summarized in Table 7 for all karst zones. With
612 the first method we evaluated the mismatching of TCEs respect to our remote sensing-derived
613 dataset, highlighting features that are most difficult to detect using remote sensing techniques. The
614 field-based verification method, on the other hand, is a measure of the quality and accuracy of our
615 remote sensing-derived CCEs in providing human-accessible underground voids in unexplored
616 areas. The calculated success rate and accuracy values of our remote-sensing analysis are reported
617 in Table 8.

618

619 **Table 7.** Correspondence between remote-sensing derived CCEs, existing and explored TCEs (from
620 own explorations and literature), and verified CCEs after ground-truthing for all karst zones.

Karst zone	CCEs	TCEs	Ver CCEs	%	CCEs matching with real caves	%	CCEs not matching with real caves	%	TCEs not identified by remote sensing	%
Z1	32	26	21	65,63	21	81	0	0	5	19
Z2	30	24	7	23,33	7	29	0	0	17	71
Z3	27	nd	0	0,00	nd	nd	nd	nd	nd	nd
Z4	38	13	11	28,95	11	85	0	0	2	15
Z5	153	25	27	17,65	25	93	1	3	1	4
Z6	20	nd	0	0,00	nd	nd	nd	nd	nd	nd
Z7	41	24	28	68,29	24	86	4	24	0	0
Z8	30	5	7	23,33	5	71	2	29	0	0

621

622

623 **Table 8.** Calculated success rates of the remote-sensing derived CCE dataset.

Testing		Success rate (%)	Average accuracy (%)
TCEs inventory verification	Z1	81	71
	Z2	29	
	Z4	85	
	Z5	93	
CCEs field verification	Z7	86	83
	Z8	71	

624

625 In Z1, among the 26 known true cave entrances, 21 were detected in our CCE inventory, whereas 5
626 points were not mapped with our image analysis. This mismatching was related to entrances
627 consisting in underground meanders developing under rock ledges on the convex (outer) side of the
628 meander's sinuosity, or narrow fissure openings on vertical cliff faces. In Z2, almost all the
629 explored TCEs are relative to very small cut-through caves, sometimes developed under the cover
630 of large dunes bodies or partially infilled by sediments (Padovan, 2007; Sesiano, 2007). Therefore,
631 17 TCEs were not correspondent to CCEs, resulting in a local success rate of only 29%. In Z4 and
632 Z5 on the other hand, almost all the points were correspondent to TCEs, with average success rates
633 respectively of 85% and 93% covering the most significant karst systems of the CDS (Padovan,
634 2015).

635 In the last two areas, Z7 and Z8, the success rates were of 86% and 71% respectively, and made it
636 possible to access and explore almost 2 km of new cave passages in Z7, and more than 1 km of new
637 cave passages in Z8. The high rate of success (average of 83%) depicts a strong reliability of the
638 proposed CCEs dataset in giving access to real cave entrances. In these two areas, all the verified
639 points that were not consistent with accessible true cave entrances (6 points) were small depressions
640 (up to 1-2 m deep) blocked by salt rock boulders and/or sediments (Fig.2b).

641 From a speleological point of view, out of the 371 mapped CCEs, only 101 were verified up to now
642 (Table 4), most of which eventually giving access to a cave passage, for a total length of over 22 km
643 of explored caves systems. With an average CCEs success rate of 83%, and an average length of
644 218 m/CCE, this would leave over 200 unexplored caves in the CDS with an estimated length of
645 nearly 50 km of underground unknown passages. Since large drainage networks often give rise to

646 large caves but with less meandering behavior (and thus shorter cave passages), the still unexplored
647 small riverbeds disappearing underground might well allow to enter narrower, but longer cave
648 systems. This is especially true for those CCEs that are located at the borders of extensive (thick)
649 salt beds. Future expeditions targeting the most promising areas will surely lead to the discovery of
650 other important salt caves.

651 This remote sensing workflow has shown to be particularly reliable in identifying CCEs and,
652 consequently, explorable caves in the CDS. Similar studies might also be carried out on terrestrial
653 volcanic terrains for the mapping of skylights and collapses of lava tubes and other volcanic caves
654 in arid, vegetation-free areas (e.g., the large basaltic shields in Saudi Arabia, Pint, 2006). However,
655 lava tube entrances are often very large (several meters in diameter) (Sauro et al., 2020), and are
656 generally collapses of cave roofs, easy to spot even on low resolution satellite images and where
657 vegetation is abundant. Given these large surface collapses typical of lava tubes, it is expected that
658 the results will be even more accurate than those illustrated for the salt caves in the CDS.

659 Additionally, other techniques may be performed to implement and enhance the accuracy of our
660 remote sensing cave detection method, for example using red relief image maps (RRIM) from
661 digital elevation models (Chiba et al., 2008; [Gökkaya](#) et al., 2021), or stochastic depressions
662 analysis by hydrological modeling to automatically map natural interruptions of the drainage
663 network (Lindsay and Creed, 2006). RRIM maps eliminate the dependency of shaded relief images
664 on incident light direction and emphasizes topographic convexity and [concavity](#) at the same time,
665 facilitating the identification of karst features by shading the side slopes and lightening the divides
666 of enclosed depressions. Furthermore, the use of LiDAR-derived DEMs and thermal-infrared
667 sensors combined with UAV (unmanned aerial vehicle) acquisitions at high to very-high resolution
668 (Rinker, 1975; Wynne et al., 2008; Melis et al., 2020), may improve the chance to identify sub-
669 horizontal cave entrances difficult to detect from the vertical views of satellite images.

670 Before setting foot on the Moon or Mars, a remote sensing inventory of CCEs should be acquired
671 on potential landing sites, to target the most promising areas for future planetary cave exploration

672 (Sauro et al., 2020; Titus et al., 2021a, 2021b). The most interesting potential extraterrestrial caves
673 identified on Mars and the Moon are lava tubes, but it might be worth having a look also into the
674 possible solutional caves in evaporite (sulfate) areas (Baioni et al., 2009; Parenti et al., 2020). These
675 caves have been carved by fluids and might be potential environments to look for extant (and
676 extinct) extraterrestrial microbial life forms.

677

678 **Acknowledgements**

679 The 2015 speleological expedition in the Cordillera de la Sal was organized by Commissione Grotte
680 “Eugenio Boegan” Trieste and La Venta Esplorazioni Geografiche Treviso, whereas the 2018
681 expedition was entirely guided by La Venta Esplorazioni Geografiche Treviso and benefited from a
682 National Geographic Exploration Grant (#CP-089R-17, JDW). Pleiades images were provided by
683 the European Space Agency (ESA) (© CNES (2018) distribution Airbus DS) thanks to the research
684 project "Atacama: a perfect evaporite karst Martian analogue" granted in 2018 (RITM0040485 -
685 UM-PM Project Proposal id41412, PI JDW). We thank the Remote Sensing Laboratory at ENEA-
686 Bologna for the DTM extraction and the use of PCI Geomatica software. Constructive comments by
687 two reviewers have been greatly appreciated and allowed us to improve our initial manuscript
688 substantially.

689

690 **References**

- 691 Baioni, D. (2019). Very recent karst landforms within Cagli crater, Sinus Meridiani, Mars. Italian
692 Journal of Geosciences, 138(2), 262-273.
- 693 Baioni, D., Tramontana, M., 2015. Evaporite karst in three interior layered deposits in Iani Chaos,
694 Mars. Geomorphology, 245, 15-22.
- 695 Baioni, D., Tramontana, M., 2016. Possible karst landforms in two unnamed craters in Tyrrhena
696 Terra, Mars. Planetary and Space Science, 132, 57-65.

697 Baioni, D., Tramontana, M., 2017. Possible evaporite karst in an interior layered deposit in Juventae
698 Chasma, Mars. *International Journal of Speleology*, 46(2), 181-189.

699 Baioni, D., Hajna, N.Z., Wezel, F. C., 2009. Karst landforms in a Martian evaporitic dome. *Acta*
700 *Carsologica*, 38(1), 9-18.

701 Baioni, D., Hajna, N. Z., Wezel, F. C., 2011. Karst landforms in an interior layered deposit within
702 the Coprates chasma, Mars. *Acta Carsologica*, 40(3), 473-481.

703 Becerra, J., Henríquez, S., Arriagada, C., 2014. Geología del área Salar de Atacama, región de
704 Antofagasta. Servicio Nacional de Geología y Minería, Carta Geológica de Chile, Serie Geología
705 Básica, 1.

706 Bernhardt, H., Reiss, D., Hiesinger, H., Ivanov, M. A., 2016. The honeycomb terrain on the Hellas
707 basin floor, Mars: A case for salt or ice diapirism. *Journal of Geophysical Research:*
708 *Planets*, 121(4), 714-738.

709 Bernhardt, H., Reiss, D., Ivanov, M., Hauber, E., Hiesinger, H., Clark, J. D., Orosei, R., 2019. The
710 banded terrain on northwestern Hellas Planitia: New observations and insights into its possible
711 formation. *Icarus*, 321, 171-188.

712 Bosák, P., Bruthans, J., Filippi, M., Svoboda, T., Šmíd, J., 1999. Karst and caves in salt diapirs, SE
713 Zagros Mts.(Iran). *Acta Carsologica* 28(2), 41-75.

714 Campbell, J. B., Wynne, R. H., 2011. Introduction to remote sensing. Guilford Press, New York.

715 Cavalli, M., Marchi, L., 2008. Characterisation of the surface morphology of an alpine alluvial fan
716 using airborne LiDAR. *Natural Hazards and Earth System Sciences*, 8(2), 323-333.

717 Cavalli, M., Trevisani, S., Comiti, F., Marchi, L., 2013. Geomorphometric assessment of spatial
718 sediment connectivity in small Alpine catchments. *Geomorphology*, 188, 31-41.

719 Chappaz, L., Sood, R., Melosh, H. J., Howell, K. C., Blair, D. M., Milbury, C., Zuber, M. T., 2017.
720 Evidence of large empty lava tubes on the Moon using GRAIL gravity. *Geophysical Research*
721 *Letters*, 44(1), 105-112.

722 Charrier, R., Pinto, L., Rodríguez, M. P., 2007. Tectonostratigraphic evolution of the Andean
723 Orogen in Chile. In: Moreno, T., Gibbons, W. (Eds.). The geology of Chile, Geological Society
724 of London, 21-114.

725 Cornet, T., Cordier, D., Bahers, T. L., Bourgeois, O., Fleurant, C., Mouélic, S. L., Altobelli, N,
726 2015. Dissolution on Titan and on Earth: Toward the age of Titan's karstic landscapes. Journal of
727 Geophysical Research: Planets, 120(6), 1044-1074.

728 Cushing, G., 2012. Candidate cave entrances on Mars. Journal of Cave and Karst Studies, 74, 33-
729 47.

730 Cushing, G. E., Titus, T. N., Wynne, J. J., Christensen, P. R., 2007. THEMIS observes possible
731 cave skylights on Mars. Geophysical Research Letters, 34(17), LT17201.

732 De Berardinis, P.L., 2016. Analysis of karst and cryokarst morphologies related to the mobilization
733 of fluids in the Arabia Terra Region, Mars. MSc. Thesis, University of Bologna.

734 De Waele, J., Forti, P., 2010. Salt rims and blisters: peculiar and ephemeral formations in the
735 Atacama Desert (Chile). Zeitschrift fur Geomorphologie 54, 51-67.

736 De Waele, J., Padovan, E., 2016. The salt from within. NSS News, 74(8), 4-9.

737 De Waele, J., Forti, P., Picotti, V., Galli, E., Rossi, A., Brook, G. A., Zini, L., and Cucchi, F.,
738 2009a. Cave deposits in Cordillera de la Sal (Atacama, Chile). GeoActa special publication 2, 97-
739 111, Bologna.

740 De Waele, J., Picotti, V., Zini, L., Cucchi, F., Forti, P., 2009b. Karst phenomena in the Cordillera de
741 la Sal (Atacama, Chile). GeoActa special publication 2, 113-127, Bologna.

742 De Waele, J., Carbone, C., Sanna, L., Vattano, M., Galli, E., Sauro, F., Forti, P., 2017. Secondary
743 minerals from salt caves in the Atacama Desert (Chile): a hyperarid and hypersaline environment
744 with potential analogies to the Martian subsurface. International Journal of Speleology, 46(1),
745 51-66.

746 De Waele, J., Pisani, L., Pastore, C., Vattano, M., 2019. Leggere le grotte nel sale di Atacama
747 (Cile). Speleologia, 81, 44-51.

748 De Waele, J., Picotti, V., Martina, M. L., Brook, G., Yang, L., Forti, P., 2020. Holocene evolution
749 of halite caves in the Cordillera de la Sal (Central Atacama, Chile) in different climate
750 conditions. *Geomorphology*, 370, 107398.

751 Dingman, R. J., 1962. Tertiary salt domes near San Pedro de Atacama, Chile. US Geological
752 Survey Professional Paper, 450, D92-D94.

753 Emery, W., Camps, A., 2017. Introduction to satellite remote sensing: atmosphere, ocean, land and
754 cryosphere applications. Elsevier, Amsterdam.

755 Fletcher, R., 1987. Practical methods of optimization. II ed., New York: John Wiley & Sons.

756 Florea, L.J., 2005. Using State-wide GIS data to identify the coincidence between sinkholes and
757 geologic structure. *Journal of Cave and Karst Studies*, 67(2), 120-124.

758 Frumkin, A., Pe'eri, S., Zak, I., 2021. Development of banded terrain in an active salt diapir:
759 potential analog to Mars. *Geomorphology*, 389, 107824.

760 Frumkin, A., 1998. Salt cave cross-sections and their paleoenvironmental implications.
761 *Geomorphology* 23(2-4), 183-191.

762 Fryer, S., 2005. Halite caves of the Atacama: *National Speleological Society News*, 63(11), 4-19.

763 Galve, J. P., Gutiérrez, F., Remondo, J., Bonachea, J., Lucha, P., Cendrero, A., 2009. Evaluating
764 and comparing methods of sinkhole susceptibility mapping in the Ebro Valley evaporite karst
765 (NE Spain). *Geomorphology*, 111(3-4), 160-172.

766 Galve, J.P., Gutiérrez, F., Lucha, P., Bonachea, J., Remondo, J., Cendrero, A., Gutierrez, M.,
767 Gimeno, M.J., Sánchez, J.A., 2009. Sinkholes in the salt-bearing evaporite karst of the Ebro
768 River valley upstream of Zaragoza city (NE Spain): geomorphological mapping and analysis as a
769 basis for risk management. *Geomorphology*, 108(3-4), 145-158.

770 Galve, J. P., Remondo, J., Gutiérrez, F., 2011. Improving sinkhole hazard models incorporating
771 magnitude–frequency relationships and nearest neighbor analysis. *Geomorphology*, 134(1-2),
772 157-170.

773 Gökkaya, E., Gutiérrez, F., Ferk, M., Görüm, T., 2021. Sinkhole development in the Sivas gypsum
774 karst, Turkey. *Geomorphology* 386, 107746. <https://doi.org/10.1016/j.geomorph.2021.107746>

775 Gutiérrez, F., Guerrero, J., Lucha, P., 2008. A genetic classification of sinkholes illustrated from
776 evaporite paleokarst exposures in Spain. *Environmental Geology*, 53(5), 993-1006.

777 Gutiérrez, F., Galve, J. P., Lucha, P., Castañeda, C., Bonachea, J., Guerrero, J., 2011. Integrating
778 geomorphological mapping, trenching, InSAR and GPR for the identification and
779 characterization of sinkholes: A review and application in the mantled evaporite karst of the
780 Ebro Valley (NE Spain). *Geomorphology*, 134(1-2), 144-156.

781 Gutiérrez, F., Parise, M., De Waele, J., Jourde, H., 2014. A review on natural and human-induced
782 geohazards and impacts in karst. *Earth-Science Reviews*, 138, 61-88.

783 Haneberg, W.C., Creighton, A.L., Medley, E.W., Jonas, D., 2005. Use of LiDAR to assess slope
784 hazards at the Lihir gold mine, Papua New Guinea. *Proceedings of the International Conference*
785 *on Landslide Risk Management*, Vancouver, British Columbia, May–June, 2005. A.A. Balkema,
786 Leiden. Supplementary CD.

787 Henríquez, S. M., Becerra, J., Arriagada, C., 2014. *Geología del área San Pedro de Atacama,*
788 *Región de Antofagasta. Servicio Nacional de Geología y Minería. Carta Geológica de Chile,*
789 *Serie Geología Básica*, 171(1), Scale 1:100,000.

790 Houston, J., Hartley, A. J., 2003. The central Andean west-slope rainshadow and its potential
791 contribution to the origin of hyper-aridity in the Atacama Desert. *International Journal of*
792 *Climatology*, 23, 1453-1464.

793 Isacks, B. L., 1988. Uplift of the central Andean plateau and bending of the Bolivian
794 orocline. *Journal of Geophysical Research: Solid Earth*, 93(B4), 3211-3231.

795 Jenks, G.F., 1967. The data model concept in statistical mapping. *International Yearbook of*
796 *Cartography*, 7, 186-90.

797 Jensen, J.R., 2015. *Introductory Digital Image Processing: A Remote Sensing Perspective*. Pearson
798 Education, New York.

799 Jordan, T. E., Isacks, B., Ramos, V. A., Allmendinger, R. W., 1983. Mountain building in the
800 Central Andes. *Episodes*, 3(3), 20-26.

801 Kaku, T., Haruyama, J., Miyake, W., Kumamoto, A., Ishiyama, K., Nishibori, T., Yamamoto, K.,
802 Crites, S.T., Michikami, T., Yokota, Y., Sood, R., Melosh, H.J., Chappaz, K.C., Howell, K. C.,
803 2017. Detection of intact lava tubes at Marius Hills on the Moon by SELENE (Kaguya) Lunar
804 Radar Sounder. *Geophysical Research Letters*, 44(20), 10-155.

805 L  veill  , R. J., Datta, S., 2010. Lava tubes and basaltic caves as astrobiological targets on Earth and
806 Mars: a review. *Planetary and Space Science*, 58(4), 592-598.

807 Lindsay JB, Creed IF. 2006. Distinguishing between artefact and real depressions in digital
808 elevation data. *Computers and Geosciences*, 32(8): 1192-1204. doi:10.1016/j.cageo.2005.11.002.

809 Lillesand, T., Kiefer, R. W., Chipman, J., 2015. Remote sensing and image interpretation. John
810 Wiley & Sons, Hoboken.

811 Lipar, M., Step  šnik, U., Ferk, M., 2019. Multiphase breakdown sequence of collapse doline
812 morphogenesis: An example from Quaternary aeolianites in Western Australia. *Geomorphology*,
813 327, 572-584.

814 Melis, M.T., Da Pelo, S., Erbi  , I., Loche, M., Deiana, G., Demurtas, V., Meloni, M.A., Dessi, F.,
815 Funedda, A., Scaioni, M., Scaringi, G., 2020. Thermal remote sensing from UAVs: A review on
816 methods in coastal cliffs prone to landslides. *Remote Sens.* 12, 1–29.
817 <https://doi.org/10.3390/rs12121971>

818 Menezes, D. F., Bezerra, F. H., Balsamo, F., Arcari, A., Maia, R. P., Cazarin, C.L., 2020.
819 Subsidence rings and fracture pattern around dolines in carbonate platforms–Implications for
820 evolution and petrophysical properties of collapse structures. *Marine and Petroleum Geology*,
821 113, 104113.

822 Moraga, A., Chong, G., Fortt, M.A., Henriquez, H., 1974. Estudio geol  gico del salar de Atacama,
823 Provincia de Antofagasta. *Bolet  n del Instituto de Investigaciones Geol  gicas*, Santiago (Chile),
824 29, 56 p.

825 Moyes, H., Montgomery, S., 2019. Locating cave entrances using lidar-derived local relief
826 modeling. *Geosciences*, 9(2), 98.

827 Muñoz, N., Charrier, R., Jordan, T., 2002. Interactions between basement and cover during the
828 evolution of the Salar de Atacama Basin, northern Chile. *Revista Geologica De Chile*, 29(1), 55-
829 80.

830 Nonomura, A., Hasegawa, S., Matsumoto, H., Takahashi, M., Masumoto, M., Fujisawa, K., 2019.
831 Curvature derived from LiDAR digital elevation models as simple indicators of debris-flow
832 susceptibility. *Journal of Mountain Science*, 16(1), 95-107.

833 Öztürk, M. Z., Şimşek, M., Şener, M. F., Utlu, M., 2018. GIS based analysis of doline density on
834 Taurus Mountains, Turkey. *Environmental Earth Sciences*, 77(14), 1-13.

835 Padovan, E., 2015. L'esplorazione delle grotte nella Cordillera de la Sal Salar de Atacama – Chile.
836 In: De Nitto, L., Maurano, F., Parise, M. (Eds.), *Atti del XXII Congresso Nazionale di*
837 *Speleologia. Memorie dell'Istituto Italiano di Speleologia, Serie II*(29), 617-628.

838 Palafox, L. F., Hamilton, C. W., Scheidt, S. P., Alvarez, A. M., 2017. Automated detection of
839 geological landforms on Mars using Convolutional Neural Networks. *Computers & Geosciences*,
840 101, 48-56.

841 Panno, S. V., Luman, D. E., 2018. Characterization of cover-collapse sinkhole morphology on a
842 groundwater basin-wide scale using Lidar elevation data: A new conceptual model for sinkhole
843 evolution. *Geomorphology*, 318, 1-17.

844 Parenti, C., Gutiérrez, F., Baioni, D., García-Arnay, Á., Sevil, J., Luzzi, E., 2020. Closed
845 depressions in Kotido crater, Arabia Terra, Mars. Possible evidence of evaporite dissolution-
846 induced subsidence. *Icarus*, 341, 113680.

847 Pepe, M., Parise, M., 2014. Structural control on development of karst landscape in the Salento
848 Peninsula (Apulia, SE Italy). *Acta Carsologica*, 43(1), 101-114.

849 Pint, J. J., 2006. Vulcanospeleology in Saudi Arabia. *Acta Carsologica*, 35(1), 107-119.

850 Pondrelli, M., Rossi, A. P., Le Deit, L., Schmidt, G., Pozzobon, R., Hauber, E., & Salese, F., 2019.

851 Groundwater control and process variability on the Equatorial Layered Deposits of Kotido crater,

852 Mars. *Journal of Geophysical Research: Planets*, 124, 779– 800.

853 Ramirez, R., Gardeweg, M., 1982. Hoja Toconao, Región de Antofagasta, Carta Geológica de

854 Chile, 1: 250 000. *Serv Nac Geol Miner Chile*, 54.

855 Ramos, V.A., 2009. Anatomy and global context of the Andes: Main geologic features and the

856 Andean orogenic cycle. *Backbone of the Americas: Shallow subduction, plateau uplift, and ridge*

857 *and terrane collision*, Geological Society of America, *Memoir* 204, 31-65.

858 Rinker, J. N., 1975. Airborne infrared thermal detection of caves and crevasses. *Photogrammetric*

859 *engineering and remote sensing*, 44(11), 1391-1399.

860 Rossi, R.J., 2018. *Mathematical Statistics: An Introduction to Likelihood Based Inference*. New

861 York: John Wiley & Sons.

862 Rubilar, J., Martínez, F., Arriagada, C., Becerra, J., Bascuñán, S., 2018. Structure of the Cordillera

863 de la Sal: A key tectonic element for the Oligocene-Neogene evolution of the Salar de Atacama

864 basin, Central Andes, northern Chile. *Journal of South American Earth Sciences*, 87, 200-210.

865 Saaty, T.L., 1980. *The Analytical Hierarchy Process*. New York, McGraw-Hill.

866 Saaty, R.W., 1987. The analytic hierarchy process - what it is and how it is used. *Mathematical*

867 *modelling*, 9(3-5), 161-176.

868 Saaty, T.L., 2008. Decision making with the analytic hierarchy process. *International journal of*

869 *services sciences*, 1(1), 83-98.

870 Salomon, J.-N., 1995. Le Chili. Pays des karsts extrêmes. *Karstologia*, 24, 52-56.

871 Sauro, F., Pozzobon, R., Massironi, M., De Berardinis, P., Santagata, T., De Waele, J., 2020. Lava

872 tubes on Earth, Moon and Mars: A review on their size and morphology revealed by comparative

873 planetology. *Earth-Science Reviews*, 209, 103288.

874 Sesiano, J., 1998. Phénomènes karstiques en zone aride. Le désert d'Atacama, au Nord du Chili.

875 Hypogées "Les Boueux", 64, 48-52.

876 Sesiano, J., 2006. Evolution actuelle des phénomènes karstiques dans la Cordillera de la Sal
877 (Atacama, Nord Chili). *Karstologia*, 47, 49-54.

878 Sesiano, J., 2009. Nouvelles observations sur un massif de sel gemme dans la Cordillera de la Sal,
879 désert d'Atacama, nord du Chili. *Archives des Sciences Genève*, 62, 71-86.

880 Schowengerdt, R.A., 2006. Remote sensing: models and methods for image processing. Academic
881 Press (Elsevier), Burlington.

882 Silburt, A., Ali-Dib, M., Zhu, C., Jackson, A., Valencia, D., Kissin, Y., Tamayo, D., Menou, K.,
883 2019. Lunar crater identification via deep learning. *Icarus*, 317, 27-38.

884 Titus, T. N., Wynne, J. J., Malaska, M. J., Agha-Mohammadi, A. A., Buhler, P. B., Alexander, E.
885 C., Ashley, J.W., Azua-Bustos, A., Boston, P.J., Buczkowski, D.L., Chiao, L., Cushing, G.E.,
886 DeDecker, J., de León, P., Demirel-Floyd, C., De Waele, J., Fairén, A.G., Frumkin, A., Harris,
887 G.L., Jones, H., Kerber, L.H., Leonard, E.J., Léveillé, R.J., Manyapu, K., Massironi, M., Miller,
888 A.Z., Mylroie, J.E., Onac, B.P., Parazynski, S., Phillips, C.B., Phillips-Lander, C.M., Prettyman,
889 T.H., Sapers, H.M., Sauro, F., Schorghofer, N., Schulze-Makuch, D., Scully, J.E., Uckert, K.,
890 Wagner, R.V., Whittaker, W.L., Williams, K.E., Wong, U. Y. (2021a). A roadmap for planetary
891 caves science and exploration. *Nature Astronomy*, 5(6), 524-525.

892 Titus, T. N., Wynne, J. J., Boston, P.J., de León, P., Demirel-Floyd, C., Jones, H., Sauro, F., Uckert,
893 K., Agha-Mohammadi, A. A., Alexander, E. C., Ashley, J.W., Azua-Bustos, A., Chiao, L.,
894 Cushing, G.E., DeDecker, J., Fairén, A.G., Frumkin, A., De Waele, J., Harris, G.L., Kerber,
895 L.H., Léveillé, R.J., Malaska, M. J., Manyapu, K., Massironi, M., Miller, A.Z., Mylroie, J.E.,
896 Onac, B.P., Parazynski, S., Phillips-Lander, C.M., Prettyman, T.H., Sapers, H.M., Schorghofer,
897 N., Schulze-Makuch, D., Whittaker, W.L., Williams, K.E., Wong, U. Y. (2021b). Science and
898 technology requirements to explore caves in our solar system. *Bulletin of the American*
899 *Astronomical Society*, 53(4), 167, 7.

900 Wang, H., Jiang, J., Zhang, G., 2018. CraterIDNet: An end-to-end fully convolutional neural
 901 network for crater detection and identification in remotely sensed planetary images. *Remote*
 902 *sensing*, 10(7), 1067.

903 Weishampel, J. F., Hightower, J. N., Chase, A. F., Chase, D. Z., Patrick, R. A., 2011. Detection and
 904 morphologic analysis of potential below-canopy cave openings in the karst landscape around the
 905 Maya polity of Caracol using airborne LiDAR. *Journal of Cave and Karst Studies*, 73(3), 187-
 906 196.

907 Weiss, D. K., Head, J. W., 2017. Salt or ice diapirism origin for the honeycomb terrain in Hellas
 908 basin, Mars?: Implications for the early martian climate. *Icarus*, 284, 249-263.

909 Wilkes, E., Gorler, K., 1988. Sedimentary and structural evolution of the Cordillera de la Sal. In: V
 910 Congreso Geológico Chileno, 1, Santiago de Chile, Chile, 173-188.

911 Wynne, J. J., Titus, T. N., Diaz, G. C., 2008. On developing thermal cave detection techniques for
 912 Earth, the Moon and Mars. *Earth and Planetary Science Letters*, 272(1-2), 240-250.